Disentangling new physics with quantum entanglement in $t\bar{t}$ production at future lepton colliders

Masato Arai,[1,*] Kentarou Mawatari,[2,3,4,†] and Nobuchika Okada[5,‡]

[1]*Faculty of Science, Yamagata University, Yamagata 990-8560, Japan*
[2]*Faculty of Education, Iwate University, Morioka, Iwate 020-8550, Japan*
[3]*Graduate School of Arts and Sciences, Iwate University, Morioka, Iwate 020-8550, Japan*
[4]*Graduate School of Science and Engineering, Iwate University, Morioka, Iwate 020-8550, Japan*
[5]*Department of Physics and Astronomy University of Alabama, Tuscaloosa, Alabama 35487, USA*

(Received 4 May 2026; accepted 14 August 2026; published 1 September 2026)

We investigate quantum entanglement and Bell-inequality violation in top-antitop pair production at future lepton colliders such as the International Linear Collider and multi-TeV muon colliders. Within the Standard Model (SM), the process proceeds through s-channel γ and Z exchange and exhibits characteristic spin-correlation patterns that encode a nontrivial amount of entanglement. We then examine how these features are modified in several well-motivated extensions of the SM; (i) a neutral scalar mediator that couples to charged leptons and top quarks via Yukawa interactions and contributes as an additional s-channel exchange, (ii) the minimal gauged $U(1)_{B-L}$ model, which introduces a new neutral gauge boson Z' coupling vectorially to SM fermions, and (iii) a Randall-Sundrum scenario, in which the exchange of massive Kaluza-Klein gravitons arising from a warped extra dimension induces additional spin-dependent interactions. For all cases, we evaluate quantum-information observables including the entanglement marker, the concurrence, and the maximal Clauser-Horne-Shimony-Holt parameter, and study their dependence on the center-of-mass energy, scattering angle, and model parameters. We find that, relative to the SM expectation, the entanglement is typically reduced in the scalar-mediator scenario, while sizable deviations can arise in the $U(1)_{B-L}$ and Randall-Sundrum cases for phenomenologically relevant regions of parameter space. These results demonstrate the potential of quantum-information observables as sensitive probes of new particles and their interaction patterns in future lepton colliders.

DOI: 10.1103/9yfq-wtfn

I. INTRODUCTION

Quantum entanglement is one of the most fundamental features of quantum mechanics. It refers to the phenomenon in which multiple quantum systems form a single global quantum state that cannot be described as a product of independent states of its subsystems. Although physical observables are measured locally on each subsystem, the measurement outcomes exhibit strong correlations that cannot be explained within classical physics. Such nonclassical correlations originate from the global structure of the quantum state itself. Well-known low-energy realizations of quantum entanglement include entangled photon pairs [1,2] and ultracold atomic systems [3], where highly controlled experimental environments have enabled precise tests of entanglement generation and its properties.

Quantum entanglement, however, is a universal phenomenon that arises in all systems governed by quantum mechanics and is by no means restricted to low-energy physics. In particular, heavy particles produced in high-energy processes provide a unique arena for studying entanglement; due to the short-distance nature of the interactions and the rapid decay of unstable particles, phase information and spin correlations of the quantum state can be preserved and accessed experimentally. From this perspective, high-energy scattering processes offer a new experimental and theoretical stage for exploring quantum entanglement.

Indeed, correlations among spin degrees of freedom in particle-antiparticle pair production have long been studied in high-energy physics. In processes such as top-quark pair production and electroweak reactions, the spin states of the produced particles can be reconstructed from their decay products, enabling systematic analyses of spin correlations within the density-matrix formalism [4–11]. These spin

*Contact author: arai@sci.kj.yamagata-u.ac.jp
†Contact author: mawatari@iwate-u.ac.jp
‡Contact author: okadan@ua.edu

Published by the American Physical Society under the terms of the Creative Commons Attribution 4.0 International license. Further distribution of this work must maintain attribution to the author(s) and the published article's title, journal citation, and DOI. Funded by SCOAP³.

correlations reflect the underlying interaction dynamics of the system and describe quantum correlations in a broad sense, not necessarily limited to quantum entanglement. Experimentally, spin correlations in top-antitop production have already been measured at the Tevatron in proton-antiproton collisions by the D0 and CDF collaborations [12–14], and subsequently at the Large Hadron Collider (LHC) in proton-proton collisions by the ATLAS and CMS experiments [15–19].

Building on this progress, quantum correlations in top-antitop production at the LHC, including quantum entanglement and Bell-inequality violation, have attracted considerable attention in recent years. Using Run-2 LHC data, Afik *et al.* [20] demonstrated that quantum entanglement in $t\bar{t}$ pairs can be observed with high statistical significance, marking the first proposal to measure entanglement in a quark-antiquark system and the highest-energy realization of such a study to date. Subsequent works have systematically investigated both the structure of entanglement and the conditions for Bell-inequality violation in $t\bar{t}$ production at the LHC, as well as their experimental accessibility [21–25]. Related analyses have also been extended to other massive systems at colliders, such as spin-1 W^+W^- pairs [26,27]. Importantly, recent measurements by ATLAS and CMS [28,29] have provided the first experimental evidence for entanglement in $pp \to t\bar{t}$, demonstrating the observability of quantum correlations in the Standard Model (SM) at high energies.

While top-antitop production has been extensively studied at hadron colliders such as the LHC, where a wide variety of quantum-mechanical observables have been analyzed, complementary studies have also been carried out at lepton colliders. Lepton colliders provide an exceptionally clean experimental environment, with precisely controlled initial states and production mechanisms dominated by electroweak interactions rather than strong dynamics. These features make them an ideal setting for high-precision investigations of spin correlations and quantum correlations in heavy-particle production.

Motivated by these advantages, detailed analyses of quantum spin observables in top-quark pair production at lepton colliders have been performed in recent years, clearly demonstrating their potential and relevance [30]. The clean environment and tunable kinematics of lepton colliders allow for a transparent interpretation of spin-correlation effects and provide a natural laboratory for studying quantum entanglement in $t\bar{t}$ systems.

Similar quantum-information-oriented analyses have also been carried out for other fermion-antifermion production processes at lepton colliders. In particular, systematic studies of spin correlations, quantum entanglement, and Bell-inequality violation in $\tau^+\tau^-$ production at electron-positron colliders have been proposed [31]. Recent works have further investigated the sensitivity of such measurements at facilities such as Beijing Electron-Positron Collider [32] and the proposed Super Tau-Charm Facility [33]. Tau-lepton pairs provide a well-controlled system for testing quantum correlations and for comparing how different fermion species and interaction structures influence their manifestation. More generally, quantum correlations in fermion-pair production have been analyzed using density-matrix and quantum-tomography formulations, including processes such as $f\bar{f} \to l^+l^-$ in the SM and its Standard Model effective field theory extensions, with particular attention to the phenomenologically relevant case $l = \tau$ [34].

More general and systematic approaches to quantum correlations in high-energy processes have recently been developed. Early progress in this direction explored quantum tomography of collider states, including approaches based on decay observables as well as production kinematics alone [35]. More recently, a fully automated framework was presented to construct production spin-density matrices for generic collider processes [36]. A particularly comprehensive theoretical framework for quantum correlations in fermion-pair production at lepton colliders, including spin correlations, entanglement, and Bell nonlocality, was developed in Ref. [37], where analytic expressions for the corresponding spin-density matrices were derived in a general setup with polarized beams and effective interactions. These theoretical approaches are complementary to quantum-tomography methods, which aim at reconstructing the same density matrix from experimental data. The choice of spin basis is also important for extracting quantum correlations, and optimized bases have been investigated for enhancing entanglement and Bell-inequality violation in top-antitop events at hadron and future lepton colliders [38]. Building on these developments, a number of works have performed detailed analyses of quantum-information observables such as concurrence and Bell parameters in processes involving fermion pairs [39,40], while other measures of quantum correlations beyond entanglement, such as quantum discord, have also been investigated in collider processes [41]. In a different but related direction, quantum-information aspects of top-quark systems have also been explored in bound-state configurations, such as toponium [42]. The potential of quantum-entanglement observables for discriminating different classes of new physics in fermion-pair production has also been investigated [43].

In this work, we perform a comprehensive analysis of quantum entanglement in $t\bar{t}$ production at lepton colliders such as the International Linear Collider (ILC) and multi-TeV muon colliders, within the SM and three representative scenarios involving neutral s-channel mediators: (i) A neutral scalar mediator Φ that couples to charged leptons and top quarks through Yukawa interactions; (ii) The minimal gauged $U(1)_{B-L}$ model [44–49], featuring a new vector boson Z' that couples vectorially to SM fermions; (iii) The Randall-Sundrum (RS) model [50], in which Kaluza-Klein (KK) excitations of the graviton contribute

as spin-2 s-channel mediators. These scenarios provide representative examples of scalar, vector, and tensor interactions. Our goal is not merely to quantify the amount of entanglement generated in each model, but to investigate whether quantum-information observables can reveal characteristic signatures of new paticles and their interaction patterns. By treating the SM and all new-physics scenarios on equal footing, we assess differences in entanglement and Bell-nonlocality observables among the SM and the three new-physics scenarios. We show that these observables provide additional information complementary to conventional classical observables such as total and differential cross sections.

The remainder of this paper is organized as follows. In Sec. II we present the general density-matrix framework for two spin-$\frac{1}{2}$ particles and define the quantum-information observables used in our analysis, including entanglement markers, concurrence and Bell-type quantities. The new physics scenarios considered in this work are summarized in Sec. III. In Sec. IV we derive the helicity amplitudes for $l^-l^+ \to t\bar{t}(l = e, \mu)$ in the SM and in the benchmark extensions. Numerical results for entanglement marker, concurrence and Bell-inequality violation at future lepton colliders are presented in Sec. V, and conclusions are given in Sec. VI. Appendix A presents an analytic study of a generic chiral gauge interaction, clarifying the dependence of the entanglement observables on the chiral couplings. Appendix B investigates the interference between chiral and vectorlike interactions, providing an analytic interpretation of the energy-dependent evolution of the entanglement extrema and the weakened-entanglement regions observed in the $U(1)_{B-L}$ scenario. Appendix C demonstrates that the disconnected entangled regions in the RS model originate from the characteristic angular dependence due to a single spin-2 KK graviton exchange.

II. FORMALISM: QUANTUM-INFORMATION OBSERVABLES

A. Spin density matrix and correlation coefficients

Spin correlations in a top-antitop system can only be fully specified once nine independent parameters are fixed, as is the case for any two-qubit state. A convenient way to encode these degrees of freedom is through the standard decomposition of the spin density matrix,

$$\rho = \frac{1}{4}(\mathbf{1}\otimes\mathbf{1} + \mathcal{B}_1\cdot\boldsymbol{\sigma}\otimes\mathbf{1} + \mathcal{B}_2\cdot\mathbf{1}\otimes\boldsymbol{\sigma} + \mathcal{C}\cdot\boldsymbol{\sigma}\otimes\boldsymbol{\sigma}), \tag{2.1}$$

where the vectors $\mathcal{B}_1 = (B_{1i})$ and $\mathcal{B}_2 = (B_{2i})$, with $i = 1, 2, 3$, quantify, respectively, the top and antitop polarizations along the spatial axes, and $\mathcal{C} = (C_{ij})$, with $i, j = 1, 2, 3$, contains nine parameters and encodes all possible spin-spin correlations. Here, $\boldsymbol{\sigma} = (\sigma^1, \sigma^2, \sigma^3)$ denotes the Pauli matrices. To give operational meaning to these components, one must choose a spatial triad. In what follows we adopt the customary orthonormal basis built from the top-quark momentum direction,

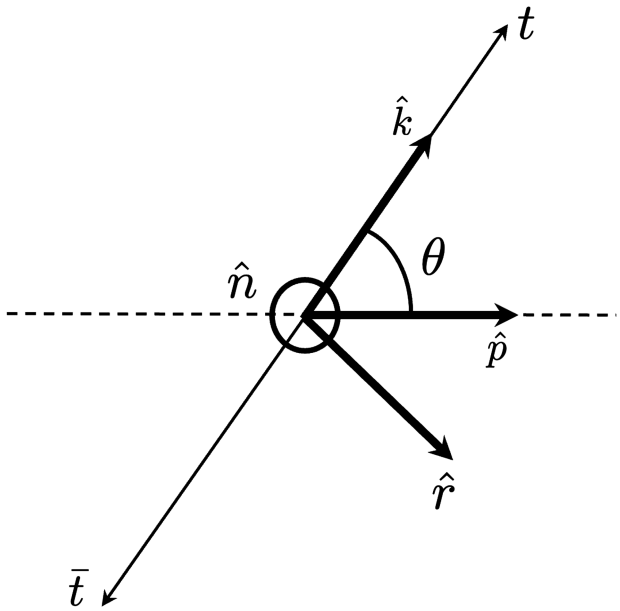


FIG. 1. Orthonormal basis $(\hat{r}, \hat{n}, \hat{k})$ in the $t\bar{t}$ rest frame, defined with respect to the top-quark direction $\hat{k}$ and beam direction $\hat{p}$.

$$\hat{k} = \text{top direction}, \qquad \hat{r} = \frac{\hat{p} - \hat{k}\cos\theta}{\sin\theta}, \qquad \hat{n} = \frac{\hat{p}\times\hat{k}}{\sin\theta}, \tag{2.2}$$

with $\hat{p}$ the incoming l^- direction, and with θ defined through $\cos\theta = \hat{k}\cdot\hat{p}$ in the $t\bar{t}$ rest frame. The geometric configuration of these vectors is depicted in Fig. 1.

B. Entanglement measures and Bell inequality

To quantify bipartite entanglement between the two spin-1/2 systems, we use the concurrence C introduced by Wootters [51]. For a given two-qubit density matrix ρ, we define the spin-flipped density matrix as

$$\tilde{\rho} = (\sigma_y \otimes \sigma_y)\rho^*(\sigma_y \otimes \sigma_y), \tag{2.3}$$

where the asterisk denotes complex conjugation in the computational basis. The non-Hermitian matrix,

$$R = \sqrt{\sqrt{\rho}\tilde{\rho}\sqrt{\rho}}, \tag{2.4}$$

has four real, non-negative eigenvalues λ_i $(i = 1, \ldots, 4)$, which we order such that $\lambda_1 \geq \lambda_2 \geq \lambda_3 \geq \lambda_4$. The concurrence is then given by

$$C = \max\{0, \lambda_1 - \lambda_2 - \lambda_3 - \lambda_4\}. \tag{2.5}$$

It satisfies $0 \leq C \leq 1$, with $C = 0$ if and only if the state is separable, and $C = 1$ for maximally entangled Bell states.

In collider environments, however, C is not an ideal observable. Extracting them from data typically inflates the impact of statistical fluctuations; related estimators have been shown to suffer from an intrinsic upward bias [22]. For this reason, it is advantageous to work with alternative quantities that retain sensitivity to quantum correlations while being more robust experimentally. As established in Refs. [23–25], the so-called entanglement markers can be built from the diagonal entries of $\mathcal{C}$,

$$D^{(1)} = \frac{1}{3}(C_{kk} + C_{rr} + C_{nn}), \tag{2.6}$$

$$D^{(k)} = \frac{1}{3}(C_{kk} - C_{rr} - C_{nn}), \tag{2.7}$$

$$D^{(r)} = \frac{1}{3}(-C_{kk} + C_{rr} - C_{nn}), \tag{2.8}$$

$$D^{(n)} = \frac{1}{3}(-C_{kk} - C_{rr} + C_{nn}). \tag{2.9}$$

Here, the indices $i, j = 1, 2, 3$ correspond to the orthonormal basis $(\hat{r}, \hat{n}, \hat{k})$, respectively. A convenient sufficient criterion for entanglement in (2.1) is

$$D_{\min} \equiv \min\{D^{(1)}, D^{(k)}, D^{(r)}, D^{(n)}\} < -\frac{1}{3}. \tag{2.10}$$

This inequality underlies the recent experimental demonstrations of top-quark entanglement in pp collisions [28,29], where $D^{(1)}$ becomes the smallest of the four markers near threshold.

While (2.10) is normally only sufficient, it becomes necessary when both top and antitop polarizations vanish, $\mathcal{B}_1 = \mathcal{B}_2 = 0$, and $\mathcal{C}$ is diagonal. In that case, the concurrence reduces to

$$C = \frac{1}{2}\max(0, -1 - 3D_{\min}), \tag{2.11}$$

which makes it explicit that nonzero entanglement appears precisely when $D_{\min} < -\frac{1}{3}$.

The nonlocal properties of the two-qubit state ρ can be probed by Bell inequalities. The simplest and most widely studied version is the Clauser-Horne-Shimony-Holt (CHSH) inequality [52], formulated in terms of spin measurements performed independently on the two qubits. One may imagine two distant observers, Alice and Bob, who each choose between two possible spin-measurement directions. Let Alice's choice of axes be the unit vectors $\hat{a}$ and $\hat{a}'$, and Bob's be $\hat{b}$ and $\hat{b}'$. For a given pair of measurement directions, the spin-spin correlation is defined as

$$E(\hat{a}, \hat{b}) = \mathrm{Tr}[\rho(\hat{a}\cdot\boldsymbol{\sigma}) \otimes (\hat{b}\cdot\boldsymbol{\sigma})], \tag{2.12}$$

where $\boldsymbol{\sigma} = (\sigma_x, \sigma_y, \sigma_z)$ are the Pauli matrices. The CHSH Bell parameter B is constructed as

$$B = E(\hat{a}, \hat{b}) + E(\hat{a}, \hat{b}') + E(\hat{a}', \hat{b}) - E(\hat{a}', \hat{b}'). \tag{2.13}$$

Local hidden-variable theories impose the CHSH bound [53]

$$|B| \leq 2, \tag{2.14}$$

whereas quantum mechanics allows values up to the Tsirelson limit $2\sqrt{2}$ [54]. This inequality thus provides a sharp criterion for diagnosing nonclassical correlations in a two-qubit system.

For an arbitrary mixed two-qubit state, the maximal quantum violation $B_{\max}$ obtainable by optimizing over all measurement directions can be expressed entirely in terms of the correlation matrix $\mathcal{C}$ defined in Eq. (2.1). Introducing

$$U = \mathcal{C}^{\mathrm{T}}\mathcal{C}, \tag{2.15}$$

and denoting its eigenvalues by $u_1 \geq u_2 \geq u_3 \geq 0$, the Horodecki criterion [55] states

$$B_{\max} = 2\sqrt{u_1 + u_2}, \tag{2.16}$$

and CHSH violation occurs if and only if

$$B_{\max} > 2 \Leftrightarrow u_1 + u_2 > 1. \tag{2.17}$$

In collider applications, $B_{\max}$ provides a clean and basis-independent diagnostic of the quantum nonlocality present in the spin state of the produced pair. The correlation matrix $\mathcal{C}$ can be reconstructed experimentally from angular distributions in the decay products of the top and antitop quarks, as discussed for example in [22–24]. In the present theoretical work, we compute $\mathcal{C}$ and consequently $B_{\max}$ directly from the density matrix (2.1).

C. Construction of the spin density matrix from helicity amplitudes

We now specialize the general two-qubit formalism to the process $l^-l^+ \to t\bar{t}(l = e, \mu)$ in the helicity basis. Throughout this paper, helicities are denoted by $\pm$, corresponding to $\pm\frac{1}{2}$.

We denote the helicity amplitudes for this process by $\mathcal{M}(\lambda_{l^-}, \lambda_{l^+}; \lambda_t, \lambda_{\bar{t}})$, where λ_{l^-}, λ_{l^+}, λ_t and $\lambda_{\bar{t}}$ represent the helicities of the incoming lepton, incoming antilepton, top quark, and antitop quark, respectively.

Since we consider unpolarized initial leptons, we start directly from the spin-averaged quantity. We define the (unnormalized) spin matrix of the final $t\bar{t}$ system as

$$R_{\lambda_t\lambda_{\bar{t}},\lambda_t'\lambda_{\bar{t}}'} \equiv \frac{1}{4}\sum_{\lambda_{l^-},\lambda_{l^+}} \mathcal{M}(\lambda_{l^-},\lambda_{l^+};\lambda_t,\lambda_{\bar{t}})\mathcal{M}^*(\lambda_{l^-},\lambda_{l^+};\lambda_t',\lambda_{\bar{t}}'), \tag{2.18}$$

where $(\lambda_t,\lambda_{\bar{t}})$ and $(\lambda_t',\lambda_{\bar{t}}')$ label the row and column of the 4×4 matrix R.

The normalized spin density matrix relevant for entanglement observables is obtained by dividing by the spin-summed rate,

$$\rho_{\lambda_t\lambda_{\bar{t}},\lambda_t'\lambda_{\bar{t}}'} = \frac{R_{\lambda_t\lambda_{\bar{t}},\lambda_t'\lambda_{\bar{t}}'}}{\sum_{\lambda_t,\lambda_{\bar{t}}} R_{\lambda_t\lambda_{\bar{t}},\lambda_t\lambda_{\bar{t}}}}, \tag{2.19}$$

so that $\mathrm{Tr}\rho = 1$ by construction.

Once ρ is obtained, we decompose it in the Pauli basis as in Eq. (2.1). The coefficients B_{1i}, B_{2i} and C_{ij} are extracted from ρ via

$$B_{1i} = \mathrm{Tr}[\rho(\sigma_i\otimes\mathbf{1})], \qquad B_{2j} = \mathrm{Tr}[\rho(\mathbf{1}\otimes\sigma_j)],$$
$$C_{ij} = \mathrm{Tr}[\rho(\sigma_i\otimes\sigma_j)]. \tag{2.20}$$

For practical calculations, it is convenient to write the density matrix explicitly in the helicity basis of the $t\bar{t}$ system. We choose the spin quantization axis along the top-quark momentum. We order the basis states as

$$|1\rangle = |+,-\rangle, \qquad |2\rangle = |+,+\rangle,$$
$$|3\rangle = |-,-\rangle, \qquad |4\rangle = |-,+\rangle,$$

where the first (second) entry denotes the helicity of the top (anti-top) quark. Since the spin quantization axis is defined by the top-quark momentum, the helicity of the anti-top quark is evaluated with respect to the same axis. As a result, the helicity states of the antitop quark correspond to spin projections opposite to its momentum; namely, a positive (negative) helicity antitop has a negative (positive) spin projection along its direction of motion.

In this basis, the density matrix can be written as

$$\rho = \begin{pmatrix} \rho_{+-,+-} & \rho_{+-,++} & \rho_{+-,--} & \rho_{+-,-+} \\ \rho_{++,+-} & \rho_{++,++} & \rho_{++,--} & \rho_{++,-+} \\ \rho_{--,+-} & \rho_{--,++} & \rho_{--,--} & \rho_{--,-+} \\ \rho_{-+,+-} & \rho_{-+,++} & \rho_{-+,--} & \rho_{-+,-+} \end{pmatrix}. \tag{2.21}$$

For brevity we denote these elements as ρ_{ij} $(i,j=1,\ldots,4)$. Since the density matrix is Hermitian, $\rho_{ij}=\rho_{ji}^*$, it is convenient to express the polarization vectors and the spin-correlation matrix in terms of the real and imaginary parts of the matrix elements. Using Eq. (2.20), we obtain

$$B_{1r} = 2\mathrm{Re}(\rho_{13}+\rho_{24}), \qquad B_{1n} = -2\,\mathrm{Im}(\rho_{13}+\rho_{24}),$$
$$B_{1k} = \rho_{11}+\rho_{22}-\rho_{33}-\rho_{44}, \tag{2.22}$$

$$B_{2r} = 2\mathrm{Re}(\rho_{12}+\rho_{34}), \qquad B_{2n} = -2\,\mathrm{Im}(\rho_{12}+\rho_{34}),$$
$$B_{2k} = \rho_{11}-\rho_{22}+\rho_{33}-\rho_{44}, \tag{2.23}$$

and

$$C_{rr} = 2\mathrm{Re}(\rho_{14}+\rho_{23}), \qquad C_{rn} = 2\,\mathrm{Im}(\rho_{23}-\rho_{14}),$$
$$C_{rk} = 2\mathrm{Re}(\rho_{13}-\rho_{24}), \tag{2.24}$$

$$C_{nr} = -2\,\mathrm{Im}(\rho_{14}+\rho_{23}), \qquad C_{nn} = 2\mathrm{Re}(\rho_{23}-\rho_{14}),$$
$$C_{nk} = 2\,\mathrm{Im}(\rho_{24}-\rho_{13}), \tag{2.25}$$

$$C_{kr} = 2\mathrm{Re}(\rho_{12}-\rho_{34}), \qquad C_{kn} = 2\,\mathrm{Im}(\rho_{34}-\rho_{12}),$$
$$C_{kk} = \rho_{11}-\rho_{22}-\rho_{33}+\rho_{44}. \tag{2.26}$$

In the following, the correlation coefficients C_{ij} are computed explicitly for each theoretical scenario considered in this work. To this end, in Sec. IV we evaluate the helicity amplitudes for $l^-l^+\to t\bar{t}$ in the SM and in the benchmark extensions, and construct the spin matrix R defined in Eq. (2.18). From the resulting density matrix ρ, the coefficients C_{ij} are extracted using Eqs. (2.24)–(2.26) and subsequently employed in Sec. V to evaluate the entanglement markers, the concurrence, and the maximal CHSH parameter.

III. MODELS

In this section we specify the three scenarios considered in the paper and collect the interactions relevant for $l^-l^+\to t\bar{t}(l=e,\mu)$.

A. Scalar mediator extension of the SM

We first consider the SM extended by a $SU(2)$ doublet scalar field Φ with $U(1)_Y$ charge $1/2$ that couples to a charged lepton $l=e,\mu$, and to the top quark via Yukawa interactions. The relevant Lagrangian terms are

$$\mathcal{L} \supset -m_\Phi^2\Phi^\dagger\Phi + \{-Y_l\bar{l}_L\Phi l_R - Y_t\bar{q}_L\tilde{\Phi}\mathrm{t}_R + \mathrm{H.c.}\}, \tag{3.1}$$

where $\tilde{\Phi}=i\sigma_2\Phi^*$, and Y_l and Y_t denote Yukawa couplings. We assume that Φ develops no vacuum expectation value.

In this scenario, $l^-l^+\to t\bar{t}$ receives, in addition to the SM γ and Z exchange, an s-channel scalar-exchange contribution proportional to Y_lY_t, which we will denote by $\mathcal{M}^{(\Phi)}$. Its helicity structure differs from that of vector and axial-vector exchange, and in particular allows same-helicity final states that are suppressed in the pure SM. As we will see, this feature has a direct impact on the entanglement pattern of the final-state spins.

B. Minimal gauged $U(1)_{B-L}$ model

The second scenario is the minimal gauged $U(1)_{B-L}$ extension of the SM [44–49,56]. The gauge group is enlarged to

$$SU(3)_C \times SU(2)_L \times U(1)_Y \times U(1)_{B-L}, \tag{3.2}$$

and the SM fermions carry $B-L$ charges equal to their baryon (B) minus lepton (L) number. Anomaly cancellation requires the introduction of three right-handed neutrinos. The $U(1)_{B-L}$ symmetry is spontaneously broken by a scalar field with $U(1)_{B-L}$ charge $+2$, giving mass to the new gauge boson Z' and generating Majorana masses for the right-handed neutrinos.

The gauge-kinetic terms involving the two Abelian factors are

$$\mathcal{L} \supset -\frac{1}{4}B_{\mu\nu}B^{\mu\nu} - \frac{1}{4}Z'_{\mu\nu}Z'^{\mu\nu} - \frac{\sin\chi}{2}B_{\mu\nu}Z'^{\mu\nu}, \tag{3.3}$$

where B_μ and Z'_μ are the gauge fields of $U(1)_Y$ and $U(1)_{B-L}$, respectively, and χ parametrizes kinetic mixing. After electroweak and $B-L$ symmetry breaking, the neutral gauge bosons mix into the photon, the SM Z and the heavy Z' boson. In the simplest limit of vanishing kinetic mixing at the $B-L$ breaking scale, the mass eigenstate Z' couples vectorially to fermions with strength proportional to their $B-L$ charge.

For the purposes of this work, we assume $\chi = 0$ in which the relevant couplings of Z' to leptons and top quarks are

$$\mathcal{L} \supset -g_{B-L}Q^l_{B-L}\bar{l}\gamma^\mu l Z'_\mu - g_{B-L}Q^t_{B-L}\bar{t}\gamma^\mu t Z'_\mu, \tag{3.4}$$

where g_{B-L} denotes the gauge coupling constant of the $U(1)_{B-L}$ symmetry, and $Q^l_{B-L} = -1$ and $Q^t_{B-L} = 1/3$ are the corresponding $B-L$ charges. The mass and the $U(1)_{B-L}$ coupling, $m_{Z'}$ and g_{B-L}, are treated as free parameters within the experimental bounds.

In this scenario, the $l^-l^+ \to t\bar{t}$ amplitude receives a new s-channel contribution from Z' exchange, which interferes with the SM photon and Z amplitudes. We denote this contribution by $\mathcal{M}^{(Z')}$.

C. Randall-Sundrum model

As a third benchmark scenario, we consider the RS model with a single warped extra dimension [50]. In this framework, the five-dimensional spacetime is a slice of anti-de Sitter space compactified on an $S^1/\mathbb{Z}_2$ orbifold, bounded by a Planck (UV) brane and a TeV (IR) brane. The nonfactorizable warped metric generates an exponential hierarchy between the electroweak and Planck scales, thereby providing a geometrical solution to the gauge hierarchy problem.

A characteristic feature of the RS model is that the zero-mode graviton and its KK excitations have distinct wave-function profiles along the extra dimension. While the graviton zero mode is localized near the Planck brane and couples to SM fields with the usual Planck-suppressed strength, the KK gravitons are localized toward the TeV brane. As a consequence, their couplings to SM fields residing on the TeV brane are significantly enhanced and become relevant for collider phenomenology.

The effective interaction between the KK gravitons and the SM fields can be written as [57,58]

$$\mathcal{L}_{\rm int} = -\frac{1}{\bar{M}_{\rm Pl}}T^{\mu\nu}(x)h^{(0)}_{\mu\nu}(x) - \frac{1}{\Lambda_\pi}T^{\mu\nu}(x)\sum_{n=1}^{\infty}h^{(n)}_{\mu\nu}(x), \tag{3.5}$$

where $h^{(n)}_{\mu\nu}$ denotes the n-th KK graviton mode, $T^{\mu\nu}$ is the energy-momentum tensor of the SM fields, and $\Lambda_\pi = \bar{M}_{\rm Pl}e^{-\kappa r_c \pi}$ is an effective interaction scale of order the TeV scale with $\bar{M}_{\rm Pl} = 2.4 \times 10^{18}$ GeV being the reduced Planck mass. The contribution of the graviton zero mode is negligible for collider processes, whereas each KK graviton couples to SM fields with strength suppressed only by Λ_π.

The masses of the KK gravitons are given by

$$m_n = x_n \kappa e^{-\kappa r_c \pi}, \tag{3.6}$$

where x_n are the roots of the Bessel function $J_1(x_n) = 0$, with $x_1 \simeq 3.83$, $x_2 \simeq 7.02$, $x_3 \simeq 10.17$, etc. Once the mass of the lightest KK graviton m_1 is fixed, the entire KK spectrum is determined by $m_n = m_1(x_n/x_1)$. It is convenient to trade the parameters of the RS geometry for the phenomenological input parameters m_1 and $\kappa/\bar{M}_{\rm Pl}$, with theoretical consistency requiring the five-dimensional curvature κ to be $\kappa/\bar{M}_{\rm Pl} \ll 1$, typically $\kappa/\bar{M}_{\rm Pl} \lesssim 0.1$ [58].

In the RS scenario, the process $l^-l^+ \to t\bar{t}$ receives additional contributions from s-channel exchange of virtual KK gravitons. The corresponding invariant amplitude can be written schematically as

$$\mathcal{M}^{(G)} = A(s)T^{\rm in}_{\mu\nu}(p_1,p_2)\eta^{\mu\rho}\eta^{\nu\sigma}T^{\rm out}_{\rho\sigma}(k_1,k_2), \tag{3.7}$$

with p_1 and p_2 (k_1 and k_2) denoting the momenta of the initial (final) particles, and

$$A(s) = -\frac{1}{\Lambda_\pi^2}\sum_{n=1}^{\infty}\frac{1}{s - m_n^2 + i m_n \Gamma_n}, \qquad s = (p_1+p_2)^2 = (k_1+k_2)^2, \tag{3.8}$$

where Γ_n denotes the total decay width of the nth KK graviton given by

$$\Gamma_n(h^{(n)} \to yy) = \frac{m_n x_n^2}{16\pi}\left(\frac{\kappa}{\bar{M}_{\rm pl}}\right)^2 \sum_y \Delta_n^{yy}, \tag{3.9}$$

with Δ_n^{yy} being a dimensionless coefficient for each decay mode, whose explicit forms are given by

$$\Delta_n^{\gamma\gamma} = \frac{1}{5}, \qquad \Delta_n^{gg} = \frac{8}{5}, \qquad \Delta_n^{\nu\bar{\nu}} = \frac{1}{10}, \tag{3.10}$$

$$\Delta_n^{VV} = c_V\sqrt{1-4r_V}\left(\frac{13}{12}+\frac{14}{3}r_V+4r_V^2\right), \quad (V=W,Z), \tag{3.11}$$

$$\Delta_n^{HH} = \frac{1}{30}(1-4r_H)^{5/2}, \tag{3.12}$$

$$\Delta_n^{f\bar{f}} = c_f(1-4r_f)^{3/2}\left(1+\frac{8}{3}r_f\right), \quad (f=l,q), \tag{3.13}$$

with

$$c_W = \frac{2}{5}, \qquad c_Z = \frac{1}{5}, \qquad c_l = \frac{1}{10}, \qquad c_q = \frac{3}{10}, \tag{3.14}$$

and $r_y = m_y^2/m_n^2$ for each SM particle y. Expressions for leptons and quarks are for one flavor.

The energy momentum tensors are given by

$$T_{\mu\nu}^{\text{in}} = \bar{v}(p_2,\lambda_{l^+})V_{\mu\nu}^{\text{in}}u(p_1,\lambda_{l^-}), \tag{3.15}$$

$$T_{\mu\nu}^{\text{out}} = \bar{u}(k_1,\lambda_t)V_{\mu\nu}^{\text{out}}v(k_2,\lambda_{\bar{t}}). \tag{3.16}$$

with

$$V_{\mu\nu}^{\text{in}} = \frac{1}{4}\Big[(p_1-p_2)_\mu\gamma_\nu + (p_1-p_2)_\nu\gamma_\mu + \eta_{\mu\nu}\left(-\frac{1}{2}(p_1-p_2)_\rho\gamma^\rho\right)\Big], \tag{3.17}$$

$$V_{\mu\nu}^{\text{out}} = \frac{1}{4}\Big[(k_1-k_2)_\mu\gamma_\nu + (k_1-k_2)_\nu\gamma_\mu + \eta_{\mu\nu}\left(-\frac{1}{2}(k_1-k_2)_\rho\gamma^\rho + m_t\right)\Big], \tag{3.18}$$

where γ^μ are the gamma matrices, m_t denotes the top-quark mass, $\eta_{\mu\nu} = \text{diag}(1,-1,-1,-1)$ is the Minkowski metric, and $u(p,\lambda)$ and $v(p,\lambda)$ denote helicity spinors given in Eqs. (4.6)–(4.9) in Sec. IV A.

The exchange of spin-2 KK gravitons induces characteristic angular distributions and helicity structures that are qualitatively different from those arising from scalar or vector mediators. As a result, the RS model can lead to distinctive modifications of the spin correlations and quantum-entanglement properties of the produced $t\bar{t}$ system. In our analysis, we include KK modes up to $i = 4$, since higher modes develop large decay widths and cease to appear as well-defined resonances, making their individual contributions difficult to identify.

IV. HELICITY AMPLITUDE AND DENSITY MATRIX FOR $l^-l^+ \to t\bar{t}$

In this section, we present the helicity amplitudes for $l^-l^+ \to t\bar{t}(l = e,\mu)$ in the SM and in the new-physics scenarios. The construction of the spin density matrix and quantum-information observables has been defined in Sec. II.

A. Kinematics and spinor conventions

We work in the center-of-mass frame of the incoming leptons with 4-momenta,

$$p_1^\mu = \frac{\sqrt{s}}{2}(1,0,0,1), \tag{4.1}$$

$$p_2^\mu = \frac{\sqrt{s}}{2}(1,0,0,-1), \tag{4.2}$$

$$k_1^\mu = \frac{\sqrt{s}}{2}(1,\beta\sin\theta\cos\phi,\beta\sin\theta\sin\phi,\beta\cos\theta), \tag{4.3}$$

$$k_2^\mu = \frac{\sqrt{s}}{2}(1,-\beta\sin\theta\cos\phi,-\beta\sin\theta\sin\phi,-\beta\cos\theta), \tag{4.4}$$

where

$$\beta = \sqrt{1-\frac{4m_t^2}{s}} \tag{4.5}$$

is the top-quark velocity in the center-of-mass frame. The angle θ is the scattering angle of the top quark with respect to the l^- beam, taken along the z axis. The azimuthal angle ϕ is measured around the beam axis from the x axis, so that the scattering plane is specified by the plane spanned by the incoming lepton momentum and the top-quark momentum.

We use spinors in the helicity basis for a fermion with mass m and four-momentum $p^\mu = (E,\boldsymbol{p})$, where $E = \sqrt{|\boldsymbol{p}|^2+m^2}$, given by

$$u(p,+1/2) = \begin{pmatrix} -\sqrt{E-|\mathbf{p}|}\chi(\hat{\boldsymbol{p}}) \\ -\sqrt{E+|\mathbf{p}|}\chi(\hat{\boldsymbol{p}}) \end{pmatrix}, \tag{4.6}$$

$$u(p,-1/2) = \begin{pmatrix} \sqrt{E+|\mathbf{p}|}\xi(\hat{\boldsymbol{p}}) \\ \sqrt{E-|\mathbf{p}|}\xi(\hat{\boldsymbol{p}}) \end{pmatrix}, \tag{4.7}$$

$$v(p,+1/2) = \begin{pmatrix} -\sqrt{E+|\mathbf{p}|}\xi(\hat{\boldsymbol{p}}) \\ \sqrt{E-|\mathbf{p}|}\xi(\hat{\boldsymbol{p}}) \end{pmatrix}, \tag{4.8}$$

$$v(p,-1/2) = \begin{pmatrix} \sqrt{E-|\mathbf{p}|}\chi(\hat{\boldsymbol{p}}) \\ -\sqrt{E+|\mathbf{p}|}\chi(\hat{\boldsymbol{p}}) \end{pmatrix}, \tag{4.9}$$

where $\hat{\boldsymbol{p}} = \boldsymbol{p}/|\boldsymbol{p}|$ is the direction of the three-momentum. The two-component helicity spinors are

$$\chi(\hat{\boldsymbol{p}}) = \begin{pmatrix} \cos\frac{\theta}{2} \\ e^{i\phi}\sin\frac{\theta}{2} \end{pmatrix}, \qquad \xi(\hat{\boldsymbol{p}}) = \begin{pmatrix} -e^{-i\phi}\sin\frac{\theta}{2} \\ \cos\frac{\theta}{2} \end{pmatrix}, \quad (4.10)$$

with (θ, ϕ) the polar and azimuthal angles of $\hat{\boldsymbol{p}}$. For the present calculation, we choose the scattering plane to coincide with the x-z plane. Accordingly, the initial lepton and antilepton are taken along the $+z$ and $-z$ directions, corresponding to $(\theta, \phi) = (0, 0)$ and $(\pi, 0)$, respectively. The final-state top quark is assigned $(\theta, \phi) = (\theta, 0)$, while the antitop quark is assigned $(\pi - \theta, \pi)$. This choice entails no loss of generality, since the azimuthal dependence is absorbed into the definition of the orthonormal basis $(\hat{r}, \hat{n}, \hat{k})$ introduced in Eq. (2.2). Consequently, all spin-dependent observables depend only on the polar angle θ.

Our convention for the fermion spinors is based on the HELAS convention [59]. However, it differs from the HELAS convention by an overall sign in the right-handed particle spinors. This difference originates from a convention-dependent phase choice in the definition of the spinors. In the present work, we adopt a convention in which this sign is explicitly retained. With this choice, the resulting density matrix satisfies the relation,

$$R_{\lambda_t\lambda_{\bar{t}},\lambda_t'\lambda_{\bar{t}}'} = R_{\lambda_{\bar{t}}\lambda_t,\lambda_{\bar{t}}'\lambda_t'}. \quad (4.11)$$

if the interaction is CP invariant [5]. Although the interactions considered in this work are not CP invariant, we adopt this convention so that the above relation holds in the CP-conserving limit, such as in QCD.

B. SM, scalar, Z' and graviton contributions to the amplitude

The full helicity amplitude can be written as

$$\mathcal{M}(\lambda_{l^-}, \lambda_{l^+}; \lambda_t, \lambda_{\bar{t}}) = \mathcal{M}^{(\mathrm{SM})}(\lambda_{l^-}, \lambda_{l^+}; \lambda_t, \lambda_{\bar{t}}) + \mathcal{M}^{(X)}(\lambda_{l^-}, \lambda_{l^+}; \lambda_t, \lambda_{\bar{t}}). \quad (4.12)$$

As introduced above, we denote the helicities $-1/2$ and $+1/2$ by $-$ and $+$, respectively. Here $\mathcal{M}^{(\mathrm{SM})}$ denotes the SM contribution, while $\mathcal{M}^{(X)}$ represents the contribution from physics beyond the SM, with $X = \Phi$ for the scalar mediator, $X = Z'$ for the $U(1)_{B-L}$ model, and $X = G$ for the RS scenario, respectively.

The first term in the right-hand side is of SM, which is given by

$$\mathcal{M}^{(\mathrm{SM})}(+,-;\pm,\pm) = \sqrt{1-\beta^2}\sin\theta\left[e^2Q_lQ_t + \frac{sg_Z^{Rl}}{2}\frac{g_Z^{Lt}+g_Z^{Rt}}{s-m_Z^2+im_Z\Gamma_Z}\right], \quad (4.13)$$

$$\mathcal{M}^{(\mathrm{SM})}(-,+;\pm,\pm) = -\sqrt{1-\beta^2}\sin\theta\left[e^2Q_lQ_t + \frac{sg_Z^{Ll}}{2}\frac{g_Z^{Lt}+g_Z^{Rt}}{s-m_Z^2+im_Z\Gamma_Z}\right], \quad (4.14)$$

$$\mathcal{M}^{(\mathrm{SM})}(+,-;\pm,\mp) = (1\pm\cos\theta)\left[e^2Q_lQ_t + \frac{sg_Z^{Rl}}{2}\frac{g_Z^{Lt}(1\mp\beta)+g_Z^{Rt}(1\pm\beta)}{s-m_Z^2+im_Z\Gamma_Z}\right], \quad (4.15)$$

$$\mathcal{M}^{(\mathrm{SM})}(-,+;\pm,\mp) = (1\mp\cos\theta)\left[e^2Q_lQ_t + \frac{sg_Z^{Ll}}{2}\frac{g_Z^{Lt}(1\mp\beta)+g_Z^{Rt}(1\pm\beta)}{s-m_Z^2+im_Z\Gamma_Z}\right], \quad (4.16)$$

where m_Z and Γ_Z is the mass and the decay width of Z boson, and

$$Q_l = -1, \qquad Q_t = \frac{2}{3}, \quad (4.17)$$

$$g_Z^{La} = \frac{e}{\cos\theta_W\sin\theta_W}(T_3^a - Q_a\sin^2\theta_W),$$
$$g_Z^{Ra} = -\frac{eQ_a\sin\theta_W}{\cos\theta_W}, \quad (4.18)$$

with $a = l$, t and

$$T_3^l = -\frac{1}{2}, \qquad T_3^t = \frac{1}{2}. \quad (4.19)$$

The additional contributions from the scalar are as follows:

$$\mathcal{M}^{(\Phi)}(\pm,\pm;\pm,\pm) = -\frac{s}{2}\frac{Y_lY_t(1-\beta)}{s-m_\Phi^2+im_\Phi\Gamma_\Phi}, \quad (4.20)$$

$$\mathcal{M}^{(\Phi)}(\pm,\pm;\mp,\mp) = \frac{s}{2}\frac{Y_lY_t(1+\beta)}{s-m_\Phi^2+im_\Phi\Gamma_\Phi}, \quad (4.21)$$

For the benchmark choice $m_\Phi = 200$ GeV adopted in our numerical analysis, the channel $\Phi \to t\bar{t}$ is closed kinematically, and we assume no other relevant decay modes. Hence Φ decays only into $l^-l^+(l = e, \mu)$, so that

$$\Gamma_\Phi \simeq \Gamma(\Phi \to l^- l^+) = \frac{|Y_l|^2 m_\Phi}{16\pi}. \tag{4.22}$$

For the $U(1)_{B-L}$ scenario, we have

$$\mathcal{M}^{(Z')}(\pm,\mp;+,+) = \pm\sqrt{1-\beta^2}\sin\theta\frac{s g_{B-L}^2 Q_{B-L}^l Q_{B-L}^t}{s - m_{Z'}^2 + i m_{Z'}\Gamma_{Z'}}, \tag{4.23}$$

$$\mathcal{M}^{(Z')}(\pm,\mp;-,-) = \pm\sqrt{1-\beta^2}\sin\theta\frac{s g_{B-L}^2 Q_{B-L}^l Q_{B-L}^t}{s - m_{Z'}^2 + i m_{Z'}\Gamma_{Z'}}, \tag{4.24}$$

$$\mathcal{M}^{(Z')}(\pm,\mp;+,-) = (1 \pm \cos\theta)\frac{s g_{B-L}^2 Q_{B-L}^l Q_{B-L}^t}{s - m_{Z'}^2 + i m_{Z'}\Gamma_{Z'}}, \tag{4.25}$$

$$\mathcal{M}^{(Z')}(\pm,\mp;-,+) = (1 \mp \cos\theta)\frac{s g_{B-L}^2 Q_{B-L}^l Q_{B-L}^t}{s - m_{Z'}^2 + i m_{Z'}\Gamma_{Z'}}, \tag{4.26}$$

where $m_{Z'}$ is the mass of Z' boson and $\Gamma_{Z'}$ is the decay width of Z' given by $\Gamma_{Z'} = \frac{13}{24\pi} g_{B-L}^2 m_{Z'}$. This has the same Lorentz structure as photon exchange but with different couplings and a massive propagator.

For the RS scenario, the additional contribution arises from s-channel exchange of KK gravitons. The corresponding helicity amplitudes can be written as

$$\mathcal{M}^{(G)}(\pm,\mp;+,+) = \mp\frac{s^2\beta}{4}A(s)\sqrt{1-\beta^2}\sin\theta\cos\theta, \tag{4.27}$$

$$\mathcal{M}^{(G)}(\pm,\mp;-,-) = \mp\frac{s^2\beta}{4}A(s)\sqrt{1-\beta^2}\sin\theta\cos\theta, \tag{4.28}$$

$$\mathcal{M}^{(G)}(\pm,\mp;+,-) = \mp\frac{s^2\beta}{8}A(s)(2\cos^2\theta \pm \cos\theta - 1), \tag{4.29}$$

$$\mathcal{M}^{(G)}(\pm,\mp;-,+) = \pm\frac{s^2\beta}{8}A(s)(2\cos^2\theta \mp \cos\theta - 1). \tag{4.30}$$

Unlike the scalar and vector mediators, the exchange of a spin-2 KK graviton induces helicity structures characteristic of its tensorial coupling to the energy-momentum tensor. As seen from Eqs. (4.27)–(4.30), the angular dependence exhibits nontrivial combinations such as $\cos^2\theta$ and $\sin\theta\cos\theta$, which are absent in scalar or vector exchanges.

Moreover, the overall energy dependence encoded in $A(s)$ differs significantly from that of scalar or vector mediators, effectively scaling as s at the amplitude level. This distinct behavior reflects the higher-dimensional origin of the interaction and can lead to qualitatively different modifications of spin correlations and entanglement observables, especially at high energies.

While the $U(1)_{B-L}$ contribution has the same Lorentz structure as photon exchange, differing only by the couplings and the massive propagator, the RS contribution represents a genuinely new tensor interaction. As a consequence, the RS scenario provides a qualitatively distinct benchmark for studying the sensitivity of quantum-entanglement observables to the spin and Lorentz structure of new physics.

V. NUMERICAL ANALYSIS

In this section we present numerical results for the entanglement marker, the concurrence, and the maximal CHSH Bell parameter in the four scenarios. The SM inputs are fixed to $\alpha = e^2/(4\pi) = 1/128$, $m_t = 173$ GeV, $\sin^2\theta_W = 0.23343$ and $m_Z = 91.188$ GeV. For the numerical analysis, we adopt representative benchmark points for each new-physics scenario, as summarized in Table I. The parameters are chosen within phenomenologically viable ranges, and the new-physics contributions lead to visible deviations from the SM. Our goal is not merely to quantify the amount of quantum correlation in each benchmark model. Rather, we investigate whether quantum-information observables can reveal characteristic signatures of new particles and the structure of their interactions. To this end, we compare scalar, vector, and tensor mediators on equal footing and examine how the distinctive features of these new particles and their interactions are encoded in the kinematic dependence of the entanglement marker, concurrence, and Bell-nonlocality observables.

We first discuss the entanglement marker, shown in Figs. 2 and 3. The contour plots reveal the kinematic regions where quantum correlations are enhanced, while the angular distributions at fixed energies provide a complementary

TABLE I. Benchmark masses and coupling parameters in the new-physics models for numerical analysis.

Model	Mediated particle	Masses [TeV]	Coupling parameters
Scalar-mediator	Φ (spin-0)	0.2	$Y_l = Y_t = 0.2$
$U(1)_{B-L}$	Z' (spin-1)	5.0	$g_{B-L} = 0.4$
RS	G (spin-2)	5.5, 10.1, 14.6, 19.1	$\kappa/\bar{M}_{\rm Pl} = 0.2$

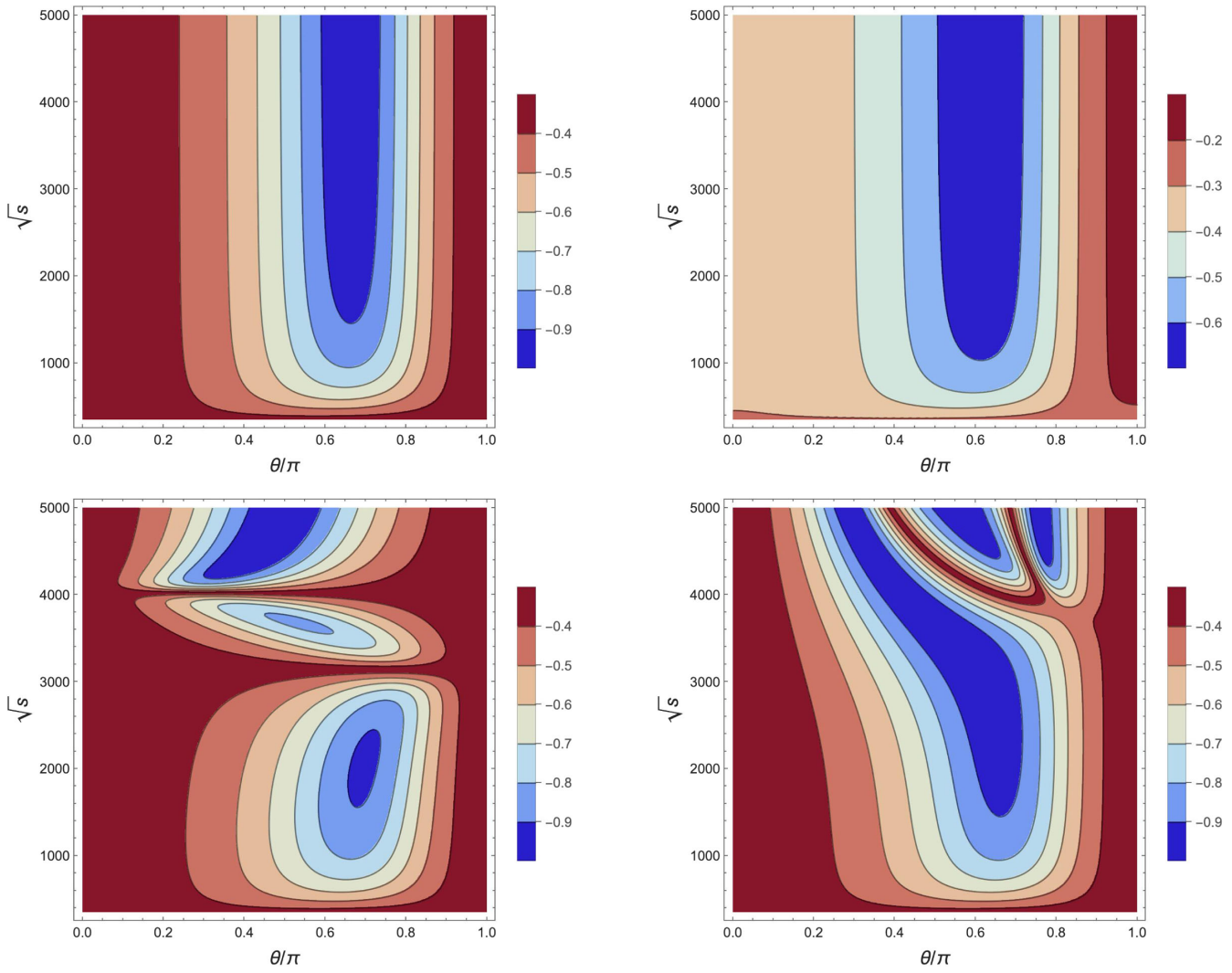


FIG. 2. Contours of the entanglement marker in the $(\sqrt{s}, \theta/\pi)$ plane. The top panels show the SM (left) and the scalar-mediator model (right), while the bottom panels show the $U(1)_{B-L}$ model (left) and the RS model (right).

one-dimensional view that makes the location and depth of the extrema more transparent.

The top-left panel in Fig. 2 shows the SM case. The entanglement marker exhibits a single connected structure, with a smooth dependence on both the scattering angle and the center-of-mass energy. The correlation is strongest in the central region, $\theta/\pi \sim 0.5$–0.7, and increases gradually with energy. This behavior is also evident in the corresponding energy slices shown in the top-left panel of Fig. 3, where a single broad minimum develops and deepens as $\sqrt{s}$ increases.

The scalar mediator scenario, shown in the top-right panels of Figs. 2 and 3, preserves the overall angular pattern of the SM, with the entanglement marker developing a broad minimum around intermediate scattering angles. Its magnitude is, however, reduced. This reduction can be understood from the helicity structure of the scalar interaction. Unlike the SM vector interactions, scalar exchange enhances like-helicity top-pair configurations, which dilute the opposite-helicity spin correlations responsible for the strong quantum correlations in the SM. Since the scalar amplitude does not interfere with the SM contribution in the massless-lepton limit, the overall topology of the distribution remains largely unchanged and no qualitatively new structures emerge. As the center-of-mass energy increases, the minimum becomes deeper while its position remains nearly unchanged. Narrow angular regions then emerge where the marker exceeds the entanglement threshold, indicating a loss of entanglement.

In contrast, the $U(1)_{B-L}$ model leads to a more intricate structure, with multiple disconnected regions appearing in the contour plots, as shown in the bottom-left panel of Fig. 2. At low energies, the contour resembles the SM pattern. At intermediate energies, a distinct entanglement extremum appears between $\sqrt{s} \simeq 3$ TeV and 4 TeV, while the entanglement is significantly weakened near these two energies. This produces the isolated entangled region observed in the contour plot. At higher energies, the entanglement extremum

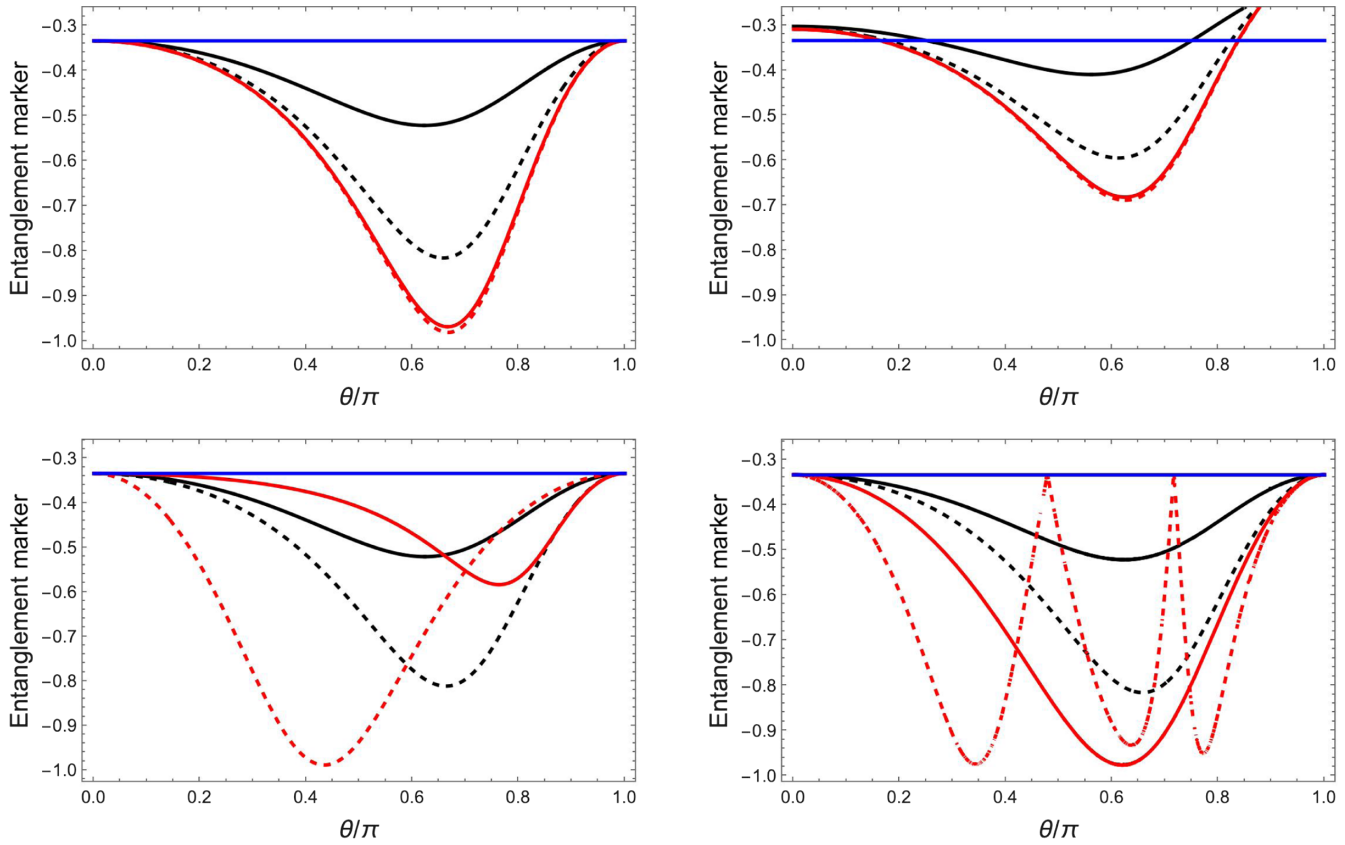


FIG. 3. Angular dependence of the entanglement marker at fixed center-of-mass energies for the SM (top left), the scalar-mediator model (top right), the $U(1)_{B-L}$ model (bottom left) and RS model. The solid black, dashed black, solid red, and dashed red curves correspond to $\sqrt{s} = 500$ GeV, 1000 GeV, 3000 GeV, and 4500 GeV, respectively. The horizontal blue line indicates the threshold below which the state is entangled.

appears around $\theta/\pi = 1/2$. The analytic interpretation of these features is presented in Appendixes A and B. Appendix A considers a generic chiral gauge interaction and explains the angular position of the entanglement extremum at low and high energies in terms of the relative strengths of the left- and right-chiral couplings. Appendix B extends this analysis by including both a chiral SM-like interaction and a vectorlike interaction. It shows that the energy dependence of the effective chiral combinations defined in (B26) and (B27) governs the motion of the entanglement extremum in the intermediate-energy region, while the weakened-entanglement regions around $\sqrt{s} \simeq 3$ TeV and 4 TeV arise from the cancellation condition, Eq. (B12), which suppresses the off-diagonal element of the density matrix.

In the corresponding energy slices shown in the bottom-left panel of Fig. 3, the angular minimum moves with $\sqrt{s}$, while its depth is strongly reduced around $\sqrt{s} \simeq 3$ TeV, in agreement with the analytic interpretation presented in Appendixes A and B.

The RS scenario, shown in the bottom-right panels of Fig. 2, exhibits a qualitatively different behavior from both the scalar and $U(1)_{B-L}$ scenarios. Unlike these models, the RS contribution originates from spin-2 KK gravitons, which contribute through tensor interactions. At relatively low energies, the contour plot exhibits a single connected region, similar to the SM behavior. As the collision energy increases, however, additional disconnected regions emerge, indicating the growing impact of the KK-graviton contribution. To clarify the origin of the disconnected angular regions, we analyze in Appendix C the contribution from the first KK graviton alone in the massless-top limit. The analysis shows that the disconnected regions arise solely from the characteristic angular dependence of the spin-2 exchange. The resulting angular distribution is symmetric about $\theta/\pi = 1/2$ as shown in Fig. 10. While the disconnected regions originate from the characteristic angular dependence of the spin-2 exchange, the full RS prediction contains an additional feature. The contours are noticeably asymmetric about $\theta/\pi = 1/2$. This asymmetry is absent for the KK-graviton contribution alone but arises from interference with the SM amplitudes, particularly the Z-boson exchange. Such features are absent in both the scalar and vector scenarios, leading to a quantum-correlation pattern that is qualitatively distinct from those found in the other benchmark models.

The same features are reflected in the corresponding energy slices shown in the bottom-right panel of Fig. 3. At relatively low energies, the angular distribution exhibits a single broad minimum, similar to the SM behavior. As the energy increases, additional local minima develop in the angular distribution. These minima correspond to the disconnected angular regions observed in the contour plots and are consistent with the spin-2 angular structure discussed in Appendix C. Their positions are further modified by interference with the SM amplitudes. The angular distributions also exhibit the same asymmetry about $\theta/\pi = 1/2$ observed in the contour plots, consistent with the interference between the KK-graviton and SM contributions.

We now turn to the concurrence. It is instructive to examine whether the qualitative differences among the scalar, vector, and RS scenarios observed in the entanglement marker persist in another entanglement observable. The concurrence are shown in Figs. 4 and 5. Overall, its behavior closely follows that of the entanglement marker, since both quantify the strength of quantum correlations. In particular, the locations of the extrema and the global structure in the contour plots are nearly identical. This correspondence is also reflected in the energy slices, where the angular dependence exhibits a similar structure, with the positions of the extrema largely aligned with those of the entanglement marker.

The main difference lies in the overall normalization, as the concurrence provides a more direct measure of entanglement. The SM and scalar cases again show a smooth single-region structure, with a single maximum in the angular distribution, as shown in the top panels of Fig. 5. The $U(1)_{B-L}$ model, shown in the bottom-left panel of Fig. 5, retains a single maximum whose position evolves with $\sqrt{s}$. The maximum is strongly suppressed at $\sqrt{s} = 3$ TeV and increases again at higher energies. In contrast, the RS scenario, shown in the bottom-right panel of Fig. 5, develops multiple local maxima, confirming the qualitatively distinct pattern already observed in the

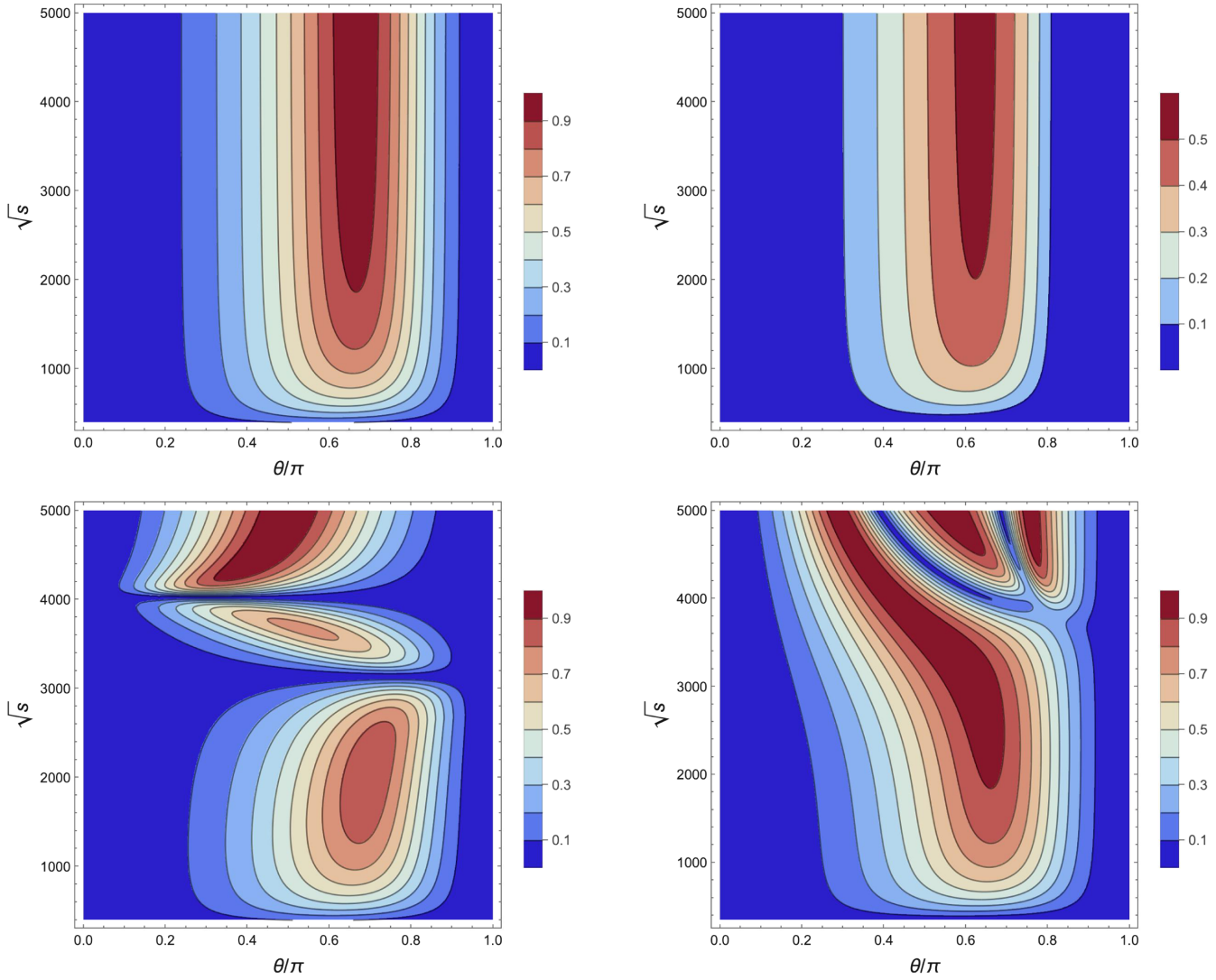


FIG. 4. Contours of the concurrence in the $(\sqrt{s}, \theta/\pi)$ plane. The panel assignments are the same as in Fig. 2 for the entanglement marker.

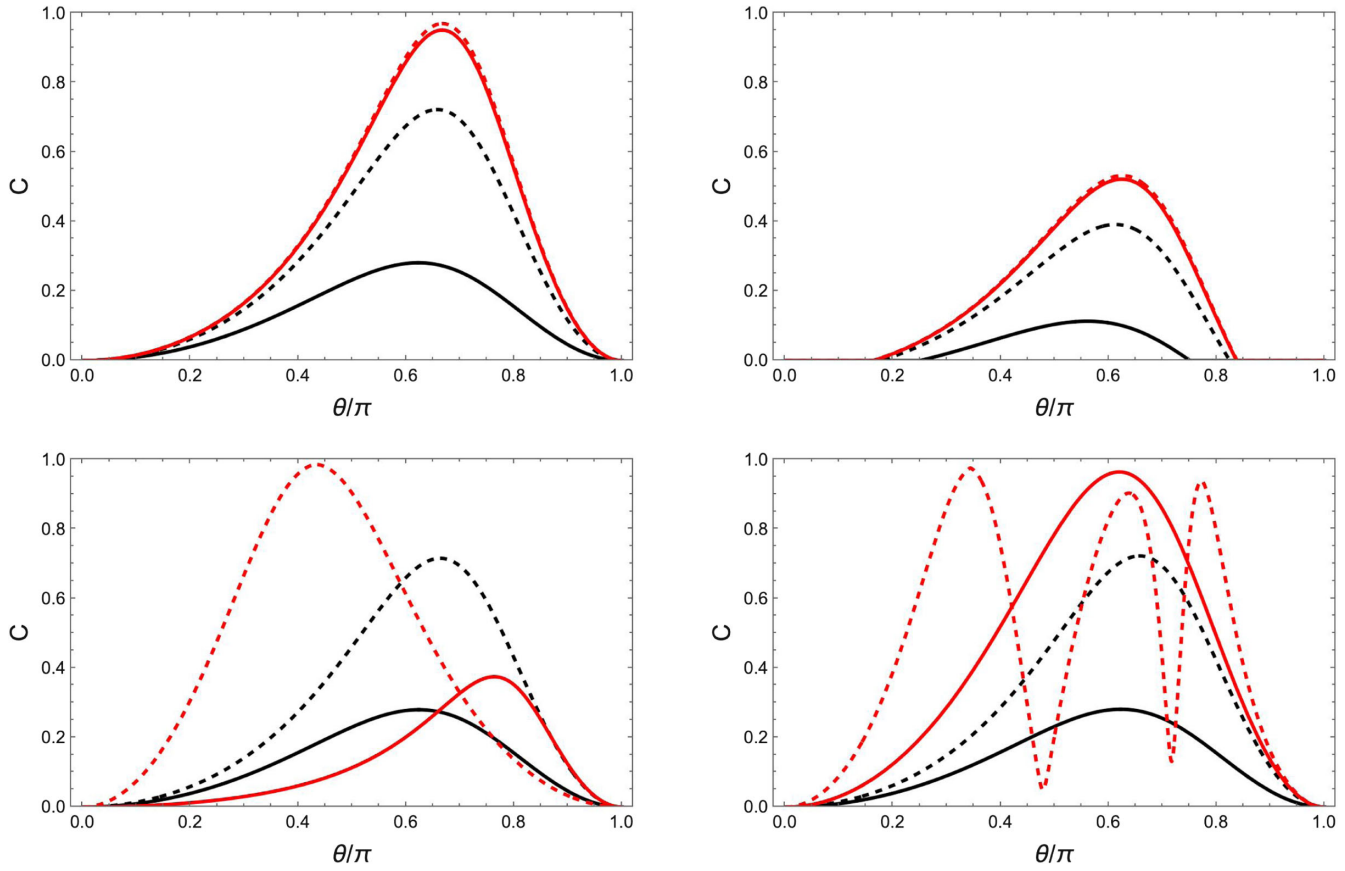


FIG. 5. Angular dependence of the concurrence at fixed center-of-mass energies. The panel assignments are the same as in Fig. 3. The solid black, dashed black, solid red, and dashed red curves correspond to $\sqrt{s} = 500$ GeV, 1000 GeV, 3000 GeV, and 4500 GeV, respectively.

entanglement marker. These observations confirm the qualitative picture obtained from the entanglement marker.

We finally turn to the maximal CHSH Bell parameter, which probes a more restrictive aspect of quantum correlations than either the entanglement marker or the concurrence. It is therefore interesting to examine whether the qualitative differences among the scalar, vector, and RS scenarios persist at the level of Bell nonlocality. The plots of the CHSH Bell parameter are shown in Figs. 6 and 7. The contour plots in Fig. 6 exhibit qualitative features similar to those of the entanglement marker and the concurrence, indicating that the qualitative differences among the scalar, vector, and RS scenarios persist across all three observables.

A similar correspondence is observed in the energy slices in Fig. 7. Despite probing a more restrictive aspect of quantum correlations, the Bell parameter retains the same qualitative distinctions among the scalar, vector, and RS scenarios that were observed in the entanglement marker and concurrence. In the SM case shown in the top-left panel of Fig. 7, the Bell parameter increases with energy and develops a single broad peak in the angular distribution, leading to Bell-inequality violation at sufficiently high energies. The scalar scenario in the top-right panel of Fig. 7 shows a much more limited pattern of Bell-inequality violation. For $\sqrt{s} = 500$ and 1000 GeV, the Bell parameter stays below the classical bound over the entire angular range. Only at higher energies, $\sqrt{s} = 3000$ and 4500 GeV, does $B_{\max}$ exceed 2, and then only within a narrow interval of intermediate scattering angles. The $U(1)_{B-L}$ model shown in the bottom-left panel of Fig. 7 exhibits a single peak whose angular position evolves with $\sqrt{s}$. The peak is strongly suppressed at $\sqrt{s} = 3$ TeV and increases at higher energies, following the behavior already observed in the concurrence. In contrast, the RS scenario shown in the bottom-right panel of Fig. 7 exhibits a broad enhancement at lower energies, while at higher energies the angular profile becomes increasingly structured. In particular, for $\sqrt{s} = 4500$ GeV, multiple local maxima emerge, reflecting the characteristic angular structure of the spin-2 KK-graviton exchange. These results further demonstrate that the characteristic differences among the scalar, vector, and RS scenarios are consistently reflected in all three quantum-information observables.

Taken together, the results for the entanglement marker, concurrence, and Bell parameter reveal a common pattern. The scalar scenario primarily suppresses the SM quantum correlations, while the $U(1)_{B-L}$ scenario is characterized by the energy-dependent evolution of the angular extrema

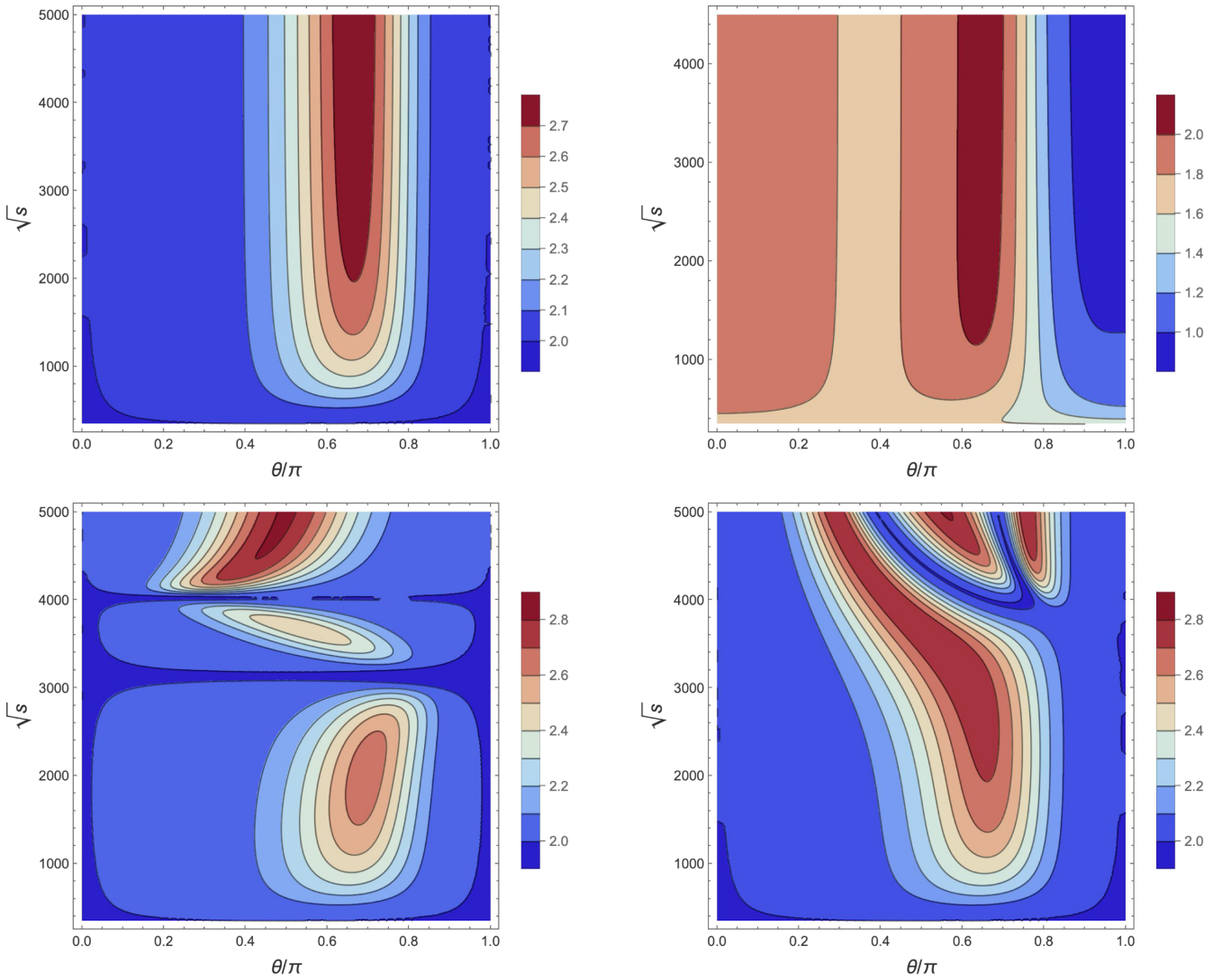


FIG. 6. Contours of the CHSH Bell parameter in the $(\sqrt{s}, \theta/\pi)$ plane. The panel assignments are the same as in Fig. 2 for the entanglement marker.

governed by the effective chiral combinations, together with the characteristic weakening of the entanglement caused by the cancellation condition. The RS scenario instead develops characteristic angular structures associated with spin-2 KK-graviton exchange, leading to qualitatively distinct signatures absent in the scalar and vector benchmarks considered here. The fact that the same qualitative distinctions among the scalar, vector, and RS scenarios are reflected in all three observables suggests that these distinctions are closely linked to the properties of the underlying new particles and their interaction patterns.

We note that all the numerical results shown in this section were confirmed by automated simulation of event-by-event spin-density matrices [36] in the MadGraph5_aMC@NLO (MadGraph hereafter) framework [60]. As a reference, we show Tables II and III, where we compare the diagonal components of the spin-correlation matrix C_{ij} and the entanglement markers $D^{(i)}$ obtained from the analytical calculation (Theory) and from the numerical simulation by MadGraph. Here, for simplicity, we isolate the contributions of each new-physics scenario from the SM contribution, and show the results for the benchmarks defined in Table I at $\sqrt{s} = 3000$ GeV with 10^5 generated events for simulation. For simulations in the scalar-mediator (spin-0) model and the RS (spin-2) model, we employ the `Higgs Characterisation` (HC) model [61], while for simulations in the $U(1)_{B-L}$ (spin-1) model, we use the `U1XGeneric` model [62]. For the RS case, we only include the contribution from the first KK graviton mode for the comparison tables. We find good agreement between the two approaches within statistical uncertainties, providing a nontrivial cross-check of the analytical framework.

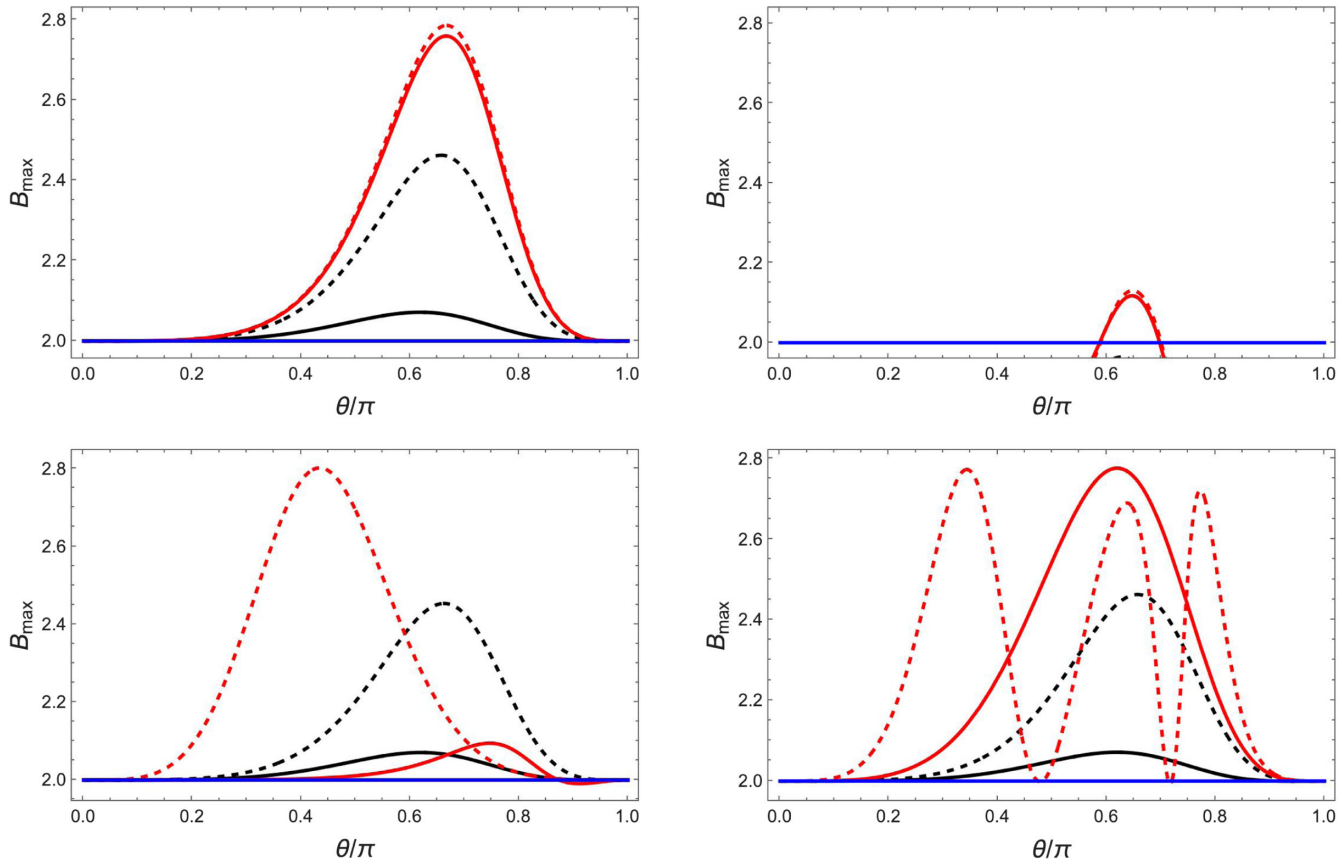


FIG. 7. Angular dependence of the CHSH Bell parameter at fixed center-of-mass energies. The panel assignments are the same as in Fig. 3. The solid black, dashed black, solid red, and dashed red curves correspond to $\sqrt{s} = 500$ GeV, 1000 GeV, 3000 GeV, and 4500 GeV, respectively. The horizontal blue line marks the classical CHSH bound $B_{\max} = 2$.

TABLE II. Comparison of the diagonal components of the spin-correlation matrix between the analytical calculation (Theory) and the numerical simulation by MadGraph.

	C_{rr}		C_{nn}		C_{kk}	
Model	Theory	MadGraph	Theory	MadGraph	Theory	MadGraph
SM	0.300	0.298	−0.290	−0.287	0.989	0.990
Scalar-mediator	−0.007	−0.007	−0.007	−0.007	−1.000	−1.000
$U(1)_{B-L}$	0.503	0.502	−0.490	−0.489	0.987	0.987
RS	−0.156	−0.158	0.174	0.176	0.982	0.982

TABLE III. Comparison of the entanglement markers $D^{(i)}$ obtained from the analytical calculation (Theory) and the numerical simulation byMadGraph.

	$D^{(1)}$		$D^{(k)}$		$D^{(r)}$		$D^{(n)}$	
Model	Theory	MadGraph	Theory	MadGraph	Theory	MadGraph	Theory	MadGraph
SM	0.333	0.333	0.326	0.326	−0.133	−0.135	−0.526	−0.525
Scalar-mediator	−0.338	−0.338	−0.329	−0.329	0.333	0.333	0.333	0.333
$U(1)_{B-L}$	0.333	0.333	0.325	0.325	0.002	0.002	−0.660	−0.660
RS	0.333	0.333	0.322	0.322	−0.438	−0.439	−0.217	−0.216

VI. DISCUSSION AND CONCLUSIONS

In this work, we have performed a systematic study of quantum entanglement and Bell-inequality violation in $l^-l^+ \to t\bar{t}(l = e, \mu)$ at future lepton colliders such as the ILC and multi-TeV muon colliders, within the SM and three representative extensions involving scalar, vector, and tensor-mediated interactions. Working in a unified density-matrix framework, we evaluated the entanglement marker, the concurrence, and the maximal CHSH Bell parameter on equal footing.

The central result of this work is that the scalar, vector, and RS scenarios leave qualitatively distinct fingerprints in quantum-information observables. Rather than merely enhancing or suppressing entanglement, the new interactions produce qualitatively distinct patterns in the quantum-information observables, reflecting the properties of the underlying new particles and their interaction patterns. The scalar mediator leads to an overall reduction of entanglement, reflecting its tendency to enhance like-helicity top-pair configurations. The absence of strong interference with the SM amplitudes further ensures that the overall topology remains similar to the SM pattern. In contrast, the $U(1)_{B-L}$ model is characterized by the energy-dependent evolution of the angular extrema together with a characteristic weakening of the entanglement, leading to a characteristic reshaping of the entanglement pattern in the $(\theta, \sqrt{s})$ plane. The RS scenario exhibits the most distinctive behavior, developing characteristic angular structures associated with spin-2 KK-graviton exchange that are absent in the scalar and vector benchmarks considered here.

We further find that the CHSH parameter provides information complementary to that of the entanglement marker and concurrence. In the SM, as well as in the $U(1)_{B-L}$ and RS scenarios, the maximal CHSH parameter exceeds the classical bound $B_{\max} = 2$ over broad angular regions, indicating persistent Bell-inequality violation throughout much of the accessible phase space. By contrast, in the scalar-mediator model the violation is much more limited: for $\sqrt{s} = 500$ and 1000 GeV, the CHSH parameter stays below the classical bound over the entire angular range, whereas clear violation appears only at higher center-of-mass energies, where it is confined to narrow angular intervals. This behavior reflects the different ways in which the interactions considered here reshape the underlying quantum-correlation structure. The vector and RS scenarios exhibit Bell-inequality violation over broader regions of phase space, whereas the scalar contribution produces a more limited pattern that becomes visible mainly at higher energies. Taken together, the entanglement marker, concurrence, and CHSH parameter therefore provide complementary diagnostics of the properties of new particles and their interaction patterns.

Future lepton colliders provide a uniquely clean environment for probing quantum entanglement with $t\bar{t}$ final state. In particular, polarized beams would allow direct control over the initial-state helicity configuration and could significantly enhance the sensitivity to the chiral and Lorentz structure of new interactions [63]. Incorporating realistic reconstruction and detector effects will be essential for assessing the experimental feasibility of measuring these quantum-information observables in practice. Such studies will help clarify the role of quantum-information observables as probes of new physics at future lepton colliders.

ACKNOWLEDGMENTS

K. M. would like to thank Valentin Durupt, Fabio Maltoni, and Olivier Mattelaer for valuable discussions and technical help in numerical computation of spin density matrices. The work of M. A. and K. M. is supported in part by JSPS Grant-in-Aid for Scientific Research (KAKENHI) under Grants No. JP25K07275 and No. JP24K07032, respectively. The work of N. O. is supported in part by the United States Department of Energy Grants No. DE-SC0012447 and No. DE-SC0026347.

DATA AVAILABILITY

The data that support the findings of this article are not publicly available. The data are available from the authors upon reasonable request.

APPENDIX A: CHIRAL GAUGE COUPLING DEPENDENCE OF THE ENTANGLEMENT OBSERVABLES

To clarify the origin of the energy-dependent shift of the entanglement extremum observed in the $U(1)_{B-L}$ scenario as discussed in Sec. V, we consider the production of a massless fermion pair through a generic neutral vector boson with independent left- and right-chiral couplings. The interaction Lagrangian is written as

$$\mathcal{L}_{\rm int} = V_\mu[\bar{e}\gamma^\mu(g_L^e P_L + g_R^e P_R)e + \bar{t}\gamma^\mu(g_L^t P_L + g_R^t P_R)t], \tag{A1}$$

where

$$P_L = \frac{1-\gamma_5}{2}, \qquad P_R = \frac{1+\gamma_5}{2}. \tag{A2}$$

The couplings are taken to be real. We neglect the electron and top masses in order to isolate the dependence of the angular distribution on the chiral structure of the interaction. The overall propagator and normalization factors cancel in the normalized density matrix and will therefore be omitted below.

The normalized density matrix is

$$\rho(\theta) = \frac{1}{N(\theta)} \begin{pmatrix} A(\theta) & 0 & 0 & B(\theta) \\ 0 & 0 & 0 & 0 \\ 0 & 0 & 0 & 0 \\ B(\theta) & 0 & 0 & D(\theta) \end{pmatrix}, \tag{A3}$$

where

$$N(\theta) = A(\theta) + D(\theta), \tag{A4}$$

$$A(\theta) = 4(g_R^t)^2 \left[(g_R^e)^2 \cos^4 \frac{\theta}{2} + (g_L^e)^2 \sin^4 \frac{\theta}{2} \right], \tag{A5}$$

$$D(\theta) = 4(g_L^t)^2 \left[(g_L^e)^2 \cos^4 \frac{\theta}{2} + (g_R^e)^2 \sin^4 \frac{\theta}{2} \right], \tag{A6}$$

$$B(\theta) = [(g_L^e)^2 + (g_R^e)^2] g_L^t g_R^t \sin^2 \theta. \tag{A7}$$

From the density matrix (A3), we have the entanglement marker as

$$D_{\min}(\theta) = -\frac{1}{3} \left[1 + \frac{4|B(\theta)|}{N(\theta)} \right]. \tag{A8}$$

Thus, the entanglement condition (2.10) is satisfied whenever the off-diagonal element $B(\theta)$ is nonzero.

The concurrence can also be evaluated analytically. For the density matrix in Eq. (A3), we have

$$C(\theta) = \frac{2|B(\theta)|}{N(\theta)}. \tag{A9}$$

Consequently, the entanglement marker and concurrence satisfy the simple relation

$$D_{\min}(\theta) = -\frac{1 + 2C(\theta)}{3}. \tag{A10}$$

The two observables therefore contain the same angular information in the present massless single-vector-exchange limit. In particular, the minimum of $D_{\min}$ occurs at the same angle as the maximum of the concurrence.

The dependence of this angle on the chiral couplings can be obtained explicitly. Introducing

$$P = (g_R^t g_R^e)^2 + (g_L^t g_L^e)^2, \tag{A11}$$

$$Q = (g_R^t g_L^e)^2 + (g_L^t g_R^e)^2, \tag{A12}$$

and defining

$$x = \cos\theta, \tag{A13}$$

the normalization factor becomes

$$N(x) = P(1+x)^2 + Q(1-x)^2, \tag{A14}$$

whereas

$$|B(x)| = R(1-x^2), \qquad R = [(g_L^e)^2 + (g_R^e)^2]|g_L^t g_R^t|. \tag{A15}$$

It follows that

$$C(x) = \frac{2R(1-x^2)}{P(1+x)^2 + Q(1-x)^2}. \tag{A16}$$

The nontrivial extremum of (A16) in the physical angular region is located at

$$\cos\theta_{\text{ext}} = \frac{\sqrt{Q} - \sqrt{P}}{\sqrt{P} + \sqrt{Q}}. \tag{A17}$$

At this angle, the concurrence reaches

$$C_{\max} = \frac{R}{\sqrt{PQ}}, \tag{A18}$$

and the entanglement marker takes the minimum value

$$D_{\min}^{(\min)} = -\frac{1}{3} \left(1 + \frac{2R}{\sqrt{PQ}} \right). \tag{A19}$$

Equation (A17) shows explicitly that the angular position of the entanglement structure is controlled by the relative strengths of the chiral couplings. The distribution is symmetric about $\theta = \pi/2$ when

$$P = Q. \tag{A20}$$

Indeed,

$$P - Q = [(g_R^t)^2 - (g_L^t)^2][(g_R^e)^2 - (g_L^e)^2]. \tag{A21}$$

Therefore, $P = Q$ if the coupling to either the initial or final fermion is vectorlike in magnitude. In particular, for the $U(1)_{B-L}$ interaction,

$$g_L^e = g_R^e, \qquad g_L^t = g_R^t, \tag{A22}$$

and one obtains

$$\theta_{\text{ext}} = \frac{\pi}{2}. \tag{A23}$$

By contrast, if $P > Q$, the extremum is shifted to $\theta > \pi/2$, while for $P < Q$ it is shifted to $\theta < \pi/2$.

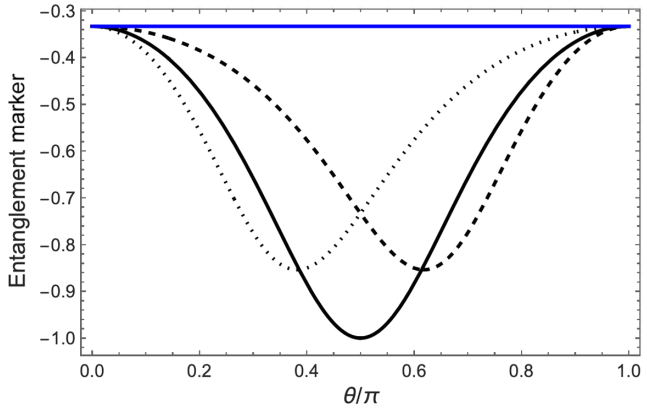


FIG. 8. Angular dependence of the entanglement marker for several representative choices of chiral couplings. The blue horizontal line denotes the separability bound, $D_{\min} = -1/3$. The solid curve corresponds to vectorlike couplings $P = Q$, $(g_R^e = g_L^e = g_R^t = g_L^t = 1)$, while the dashed and dotted curves illustrate the cases $P > Q(g_R^l = g_R^t = 3, g_L^l = g_L^t = 1)$ and $P < Q(g_R^l = g_R^t = 1, g_L^l = g_L^t = 3)$, respectively. The minimum shifts according to Eq. (A17), demonstrating that its angular position is determined by the relative strengths of the left- and right-chiral couplings. couplings.

We show the dependence of the entanglement marker on the chiral couplings in Fig. 8. For vectorlike couplings, $P = Q$, and the minimum is located at $\theta = \pi/2$. When $P > Q$, the minimum is shifted towards $\theta > \pi/2$, whereas $P < Q$ shifts the minimum towards $\theta < \pi/2$, in complete agreement with Eq. (A17).

These results provide a simple interpretation of the energy-dependent angular structures found in the full $U(1)_{B-L}$ calculation. At relatively low energies, the distribution is dominated by the SM amplitudes and reflects their chiral asymmetry. In the energy region where the Z' contribution dominates, the vectorlike $U(1)_{B-L}$ couplings drive the entanglement extremum toward the symmetric position $\theta/\pi = 1/2$. The energy-dependent movement of the entanglement extrema and the weakened-entanglement regions observed in the intermediate-energy region require the coexistence of chiral and vectorlike interactions. These features are analyzed in Appendix B.

APPENDIX B: ANALYTIC INTERPRETATION OF THE INTERMEDIATE-ENGRGY ENTANGLEMENT PATTERN IN THE $U(1)_{B-L}$ MODEL

As discussed in Sec. V, the $U(1)_{B-L}$ model exhibits two characteristic features in the intermediate-energy region. The entanglement extrema move with the collision energy, while the entanglement is significantly weakened around $\sqrt{s} \simeq 3$ TeV and 4 TeV, leading to the weakened-entanglement regions in Fig. 2. To clarify the origin of this behavior, we consider a simplified model containing a massless neutral vector boson A_μ with generic chiral couplings and a massive neutral vector boson X_μ with vectorlike couplings. The former mimics the chiral structure of the SM Z boson, with its mass neglected, whereas the latter mimics the vectorlike Z' boson of the $U(1)_{B-L}$ model. The interaction Lagrangian is

$$\mathcal{L}_{\rm int} = A_\mu[\bar{e}\gamma^\mu(g_L^l P_L + g_R^l P_R)e + \bar{t}\gamma^\mu(g_L^t P_L + g_R^t P_R)t] + g_{B-L}X_\mu(Q_{B-L}^l \bar{e}\gamma^\mu e + Q_{B-L}^t \bar{t}\gamma^\mu t). \tag{B1}$$

We neglect the lepton and top-quark masses, as in Appendix A, and also neglect the width of the massive vector boson.

The normalized density matrix takes the form

$$\rho(s,\theta) = \frac{1}{N(s,\theta)}\begin{pmatrix} A(s,\theta) & 0 & 0 & B(s,\theta) \\ 0 & 0 & 0 & 0 \\ 0 & 0 & 0 & 0 \\ B(s,\theta) & 0 & 0 & D(s,\theta) \end{pmatrix}, \tag{B2}$$

where

$$A(s,\theta) = 4\left[G_{RR}^2(s)\cos^4\frac{\theta}{2} + G_{LR}^2(s)\sin^4\frac{\theta}{2}\right], \tag{B3}$$

$$D(s,\theta) = 4\left[G_{LL}^2(s)\cos^4\frac{\theta}{2} + G_{RL}^2(s)\sin^4\frac{\theta}{2}\right], \tag{B4}$$

$$B(s,\theta) = [G_{RR}(s)G_{RL}(s) + G_{LR}(s)G_{LL}(s)]\sin^2\theta, \tag{B5}$$

$$N(s,\theta) = A(s,\theta) + D(s,\theta), \tag{B6}$$

with

$$G_{RR}(s) = g_R^l g_R^t - \chi(s), \qquad G_{LR}(s) = g_L^l g_R^t - \chi(s), \tag{B7}$$

$$G_{LL}(s) = g_L^l g_L^t - \chi(s), \qquad G_{RL}(s) = g_R^l g_L^t - \chi(s), \tag{B8}$$

and

$$\chi(s) = \frac{g_{B-L}^2}{3}\frac{s}{s - M_X^2}, \tag{B9}$$

where M_X is a mass of the X-boson. Here the factor $1/3$ follows from $Q_{B-L}^l Q_{B-L}^t = -1/3$, with an overall common sign absorbed into the definition of the four channel coefficients. The quantities $G_{RR}(s)$, $G_{LR}(s)$, $G_{LL}(s)$, and $G_{RL}(s)$ may be regarded as effective chiral couplings, since they incorporate both the original chiral couplings and the energy-dependent vectorlike contribution $\chi(s)$.

For this density matrix, the concurrence and entanglement marker are, respectively,

$$C(s,\theta) = \frac{2|B(s,\theta)|}{N(s,\theta)}, \tag{B10}$$

$$D_{\min}(s,\theta) = -\frac{1}{3}\left[1 + \frac{4|B(s,\theta)|}{N(s,\theta)}\right] = -\frac{1+2C(s,\theta)}{3}. \tag{B11}$$

The weakening of the entanglement is therefore controlled by the ratio $|B|/N$. For $\sin\theta \neq 0$, the concurrence vanishes when

$$G_{RR}(s)G_{RL}(s) + G_{LR}(s)G_{LL}(s) = 0. \tag{B12}$$

This can occur for suitable combination of gauge couplings and collision energies. In such a case, the concurrence vanishes and the entanglement marker reaches the separability bound.

Expanding Eq. (B12) in powers of χ, we obtain

$$2\chi^2 - S\chi + T = 0, \tag{B13}$$

where

$$S = (g_L^l + g_R^l)(g_L^t + g_R^t), \tag{B14}$$

$$T = [(g_L^l)^2 + (g_R^l)^2]g_L^t g_R^t. \tag{B15}$$

The solutions are

$$\chi_\pm = \frac{S \pm \sqrt{S^2 - 8T}}{4}. \tag{B16}$$

A real suppression point exists only if

$$S^2 - 8T \geq 0. \tag{B17}$$

Using Eq. (B9), the corresponding collision energies are

$$s_\pm = \frac{\chi_\pm}{\chi_\pm - g_{BL}^2/3} M_X^2, \tag{B18}$$

$$\sqrt{s_\pm} = M_X \sqrt{\frac{\chi_\pm}{\chi_\pm - g_{BL}^2/3}}. \tag{B19}$$

Conversely, for a target energy $\sqrt{s_0}$,

$$M_X = \sqrt{s_0}\sqrt{1 - \frac{g_{B-L}^2}{3\chi_\pm}}. \tag{B20}$$

A physical solution requires $\chi_\pm/(\chi_\pm - g_{BL}^2/3) > 0$.

If the massless interaction is also vectorlike,

$$g_L^l = g_R^l, \qquad g_L^t = g_R^t, \tag{B21}$$

the four coefficients in Eqs. (B7) and (B8) become identical. Away from a zero of the total production amplitude, their common energy-dependent factor cancels from the normalized density matrix. Consequently, all elements of the density matrix acquire the same energy-dependent factor, which cancels in the normalized density matrix. Therefore, purely vectorlike interactions do not generate an energy-dependent suppression of the normalized entanglement observables.

As a concrete example, let us take

$$M_X = 5\ \text{TeV}, \qquad g_{B-L} = 1, \qquad g_L^l = g_R^l = 1, \qquad g_L^t = -\frac{16}{27}, \qquad g_R^t = -\frac{3}{16}. \tag{B22}$$

For this choice,

$$\chi(3\ \text{TeV}) = -\frac{3}{16}, \qquad \chi(4\ \text{TeV}) = -\frac{16}{27}. \tag{B23}$$

The off-diagonal element becomes

$$B(s,\theta) = 2\left(-\frac{3}{16} - \chi(s)\right)\left(-\frac{16}{27} - \chi(s)\right)\sin^2\theta. \tag{B24}$$

The first factor vanishes at $\sqrt{s} = 3$ TeV, while the second factor vanishes at $\sqrt{s} = 4$ TeV. Consequently,

$$C(s,\theta) = 0, \qquad D_{\min}(s,\theta) = -\frac{1}{3} \tag{B25}$$

at these two energies for $\sin\theta \neq 0$, whereas the diagonal normalization remains nonzero. This example explicitly demonstrates that the weakening of the entanglement can arise from cancellations among the chiral-channel contributions to the off-diagonal density-matrix element.

The above analysis also provides a simple interpretation of the motion of the entanglement extrema. In particular, it explains the characteristic behavior observed in the intermediate-energy region, where the SM-like and vectorlike contributions compete. Introducing

$$P(s) = G_{RR}^2(s) + G_{LL}^2(s), \tag{B26}$$

$$Q(s) = G_{LR}^2(s) + G_{RL}^2(s), \tag{B27}$$

$$R(s) = |G_{RR}(s)G_{RL}(s) + G_{LR}(s)G_{LL}(s)|, \tag{B28}$$

the concurrence can be rewritten as

$$C(s,x) = \frac{2R(s)(1-x^2)}{P(s)(1+x)^2 + Q(s)(1-x)^2}, \qquad x = \cos\theta, \tag{B29}$$

which has the same form as Eq. (A16), with the replacements $P \to P(s)$, $Q \to Q(s)$, and $R \to R(s)$. Consequently,

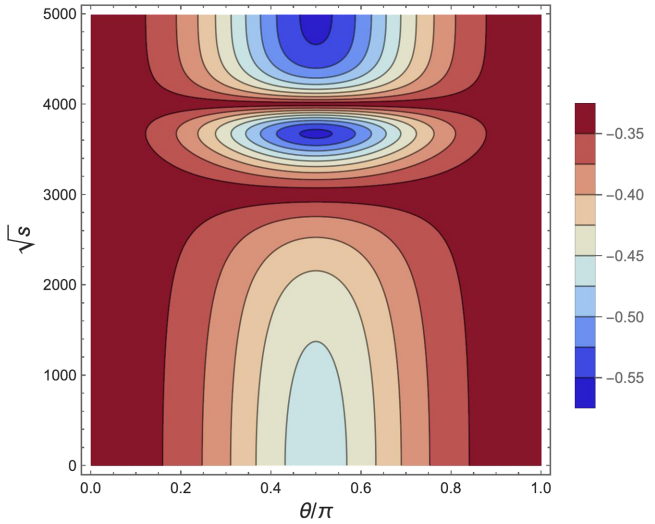


FIG. 9. Contour plot of the entanglement marker obtained from (B11) with parameters in (B22).

$$\cos\theta_{\rm ext}(s) = \frac{\sqrt{Q(s)} - \sqrt{P(s)}}{\sqrt{P(s)} + \sqrt{Q(s)}}. \tag{B30}$$

Therefore, the motion of the entanglement extrema is governed by the energy dependence of the effective chiral combinations $P(s)$ and $Q(s)$, whereas the weakening of the entanglement is controlled by the cancellation condition (B12).

Figure 9 shows the contour plot of the entanglement marker Eq. (B11) for the representative parameter set introduced in (B22). In this example, the lepton coupling is vectorlike, $g_L^l = g_R^l$, which implies $P(s) = Q(s)$ and hence $\theta_{\rm ext} = \pi/2$ at all energies. The entanglement is strongly suppressed near $\sqrt{s} = 3$ TeV and 4 TeV, where the off-diagonal density-matrix element vanishes as discussed above.

APPENDIX C: ORIGIN OF THE DISCONNECTED ENTANGLED REGIONS IN THE RS MODEL

In this Appendix, we clarify the origin of the disconnected entangled regions found in the RS model. For this purpose, we isolate the contribution from the first KK graviton and neglect the SM amplitudes. We also take the massless-top limit, $m_t = 0$, in order to extract the angular structure associated purely with the spin-2 exchange.

In this limit, the helicity amplitudes can be written schematically as

$$\mathcal{M}^{(G)}(s,\theta) = A(s)\mathcal{F}(\theta), \tag{C1}$$

where $A(s)$ is given in (3.8), while $\mathcal{F}(\theta)$ describes the angular dependence of the helicity amplitudes. Since the spin density matrix is normalized by its trace, the common factor $|A(s)|^2$ cancels. The normalized density matrix therefore depends only on the scattering angle in this simplified limit. As in Appendix A, only the $\rho_{+-,+-}$, $\rho_{+-,-+}$, $\rho_{-+,+-}$, and $\rho_{-+,-+}$ components are nonvanishing. The normalized density matrix is therefore written as

$$\rho = \frac{1}{2}\begin{pmatrix} 1 & 0 & 0 & r(\theta) \\ 0 & 0 & 0 & 0 \\ 0 & 0 & 0 & 0 \\ r(\theta) & 0 & 0 & 1 \end{pmatrix}, \tag{C2}$$

where

$$r(\theta) = \frac{2\sin\theta\sin 3\theta}{2 + \cos 2\theta + \cos 4\theta}. \tag{C3}$$

For the density matrix in Eq. (C2), the entanglement marker reduces to

$$D_{\rm min}(\theta) = -\frac{1}{3}(1 + 2|r(\theta)|). \tag{C4}$$

Thus, the entanglement marker returns to its boundary value whenever $r(\theta) = 0$. The denominator in Eq. (C3) remains positive throughout the physical angular range. Indeed,

$$2 + \cos 2\theta + \cos 4\theta = 8\left(\cos^2\theta - \frac{3}{8}\right)^2 + \frac{7}{8}, \tag{C5}$$

and the polynomial on the right-hand side has no zero for $0 \le \theta \le \pi$. The numerator vanishes at

$$\theta = 0, \qquad \frac{\pi}{3}, \qquad \frac{2\pi}{3}, \qquad \pi, \tag{C6}$$

as can be easily seen from

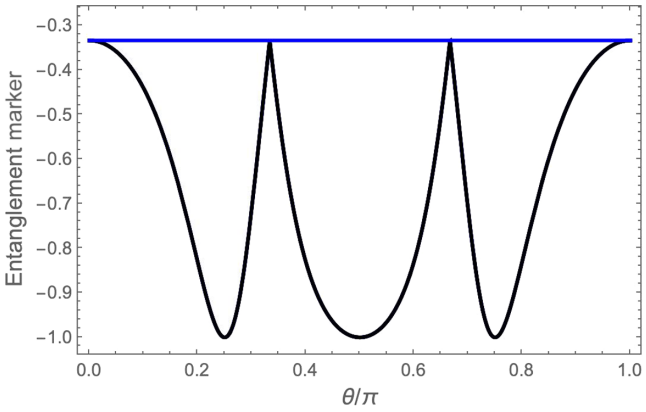


FIG. 10. Entanglement marker obtained by retaining only the first KK graviton in the massless-top limit, with the SM amplitudes omitted. The blue horizontal line denotes the separability bound, $D_{\rm min} = -1/3$, while the black curve shows the entanglement marker induced by the first KK graviton. The disconnected entangled regions are already present for a single spin-2 KK mode, demonstrating that they originate from the characteristic angular dependence of the spin-2 exchange.

$$\sin\theta \sin 3\theta = (1-\cos^2\theta)(4\cos^2\theta - 1). \quad \text{(C7)}$$

Thus, the two internal nodes at $\theta = \pi/3$ and $2\pi/3$ divide the physical angular interval into three separate regions. Therefore, the separation of the angular regions is entirely determined by the zeros of the off-diagonal matrix element $r(\theta)$.

The same conclusion follows from the concurrence. For the density matrix in Eq. (C2), the concurrence is given by

$$C(\theta) = |r(\theta)| = \left| \frac{2\sin\theta \sin 3\theta}{2 + \cos 2\theta + \cos 4\theta} \right|. \quad \text{(C8)}$$

It vanishes at the angles listed in Eq. (C6), while it becomes nonzero in the three intervening angular intervals. Note that the entanglement marker and concurrence satisfy the same relation as in (A10).

The numerical result obtained by retaining only the first KK graviton is shown in Fig. 10. The disconnected angular structure is already present in this single-mode result. This demonstrates that the multiple entangled regions are not generated by interference among different KK gravitons. Instead, they originate from the higher-order angular dependence characteristic of the spin-2 exchange, in particular from the $\sin 3\theta$ dependence of the helicity coherence.

[1] J. S. Bell, Phys. Phys. Fiz. **1**, 195 (1964).
[2] A. Aspect, P. Grangier, and G. Roger, Phys. Rev. Lett. **49**, 91 (1982).
[3] I. Bloch, J. Dalibard, and S. Nascimbène, Nat. Phys. **8**, 267 (2012).
[4] G. L. Kane, G. A. Ladinsky, and C. P. Yuan, Phys. Rev. D **45**, 124 (1992).
[5] W. Bernreuther and A. Brandenburg, Phys. Rev. D **49**, 4481 (1994).
[6] S. J. Parke and Y. Shadmi, Phys. Lett. B **387**, 199 (1996).
[7] W. Bernreuther, M. Flesch, and P. Haberl, Phys. Rev. D **58**, 114031 (1998).
[8] W. Bernreuther, A. Brandenburg, Z. G. Si, and P. Uwer, Nucl. Phys. **B690**, 81 (2004).
[9] P. Uwer, Phys. Lett. B **609**, 271 (2005).
[10] M. Baumgart and B. Tweedie, J. High Energy Phys. 03 (2013) 117.
[11] W. Bernreuther, D. Heisler, and Z. G. Si, J. High Energy Phys. 12 (2015) 026.
[12] T. Aaltonen *et al.* (CDF Collaboration), Phys. Rev. D **83**, 031104 (2011).
[13] V. M. Abazov *et al.* (D0 Collaboration), Phys. Rev. Lett. **107**, 032001 (2011).
[14] V. M. Abazov *et al.* (D0 Collaboration), Phys. Lett. B **757**, 199 (2016).
[15] G. Aad *et al.* (ATLAS Collaboration), Phys. Rev. Lett. **108**, 212001 (2012).
[16] S. Chatrchyan *et al.* (CMS Collaboration), Phys. Rev. Lett. **112**, 182001 (2014).
[17] G. Aad *et al.* (ATLAS Collaboration), Phys. Rev. Lett. **114**, 142001 (2015).
[18] A. M. Sirunyan *et al.* (CMS Collaboration), Phys. Rev. D **100**, 072002 (2019).
[19] M. Aaboud *et al.* (ATLAS Collaboration), Eur. Phys. J. C **80**, 754 (2020).
[20] Y. Afik and J. R. M. de Nova, Eur. Phys. J. Plus **136**, 907 (2021).
[21] M. Fabbrichesi, R. Floreanini, and G. Panizzo, Phys. Rev. Lett. **127**, 161801 (2021).
[22] C. Severi, C. D. Boschi, F. Maltoni, and M. Sioli, Eur. Phys. J. C **82**, 285 (2022).
[23] Y. Afik and J. R. M. de Nova, Quantum **6**, 820 (2022).
[24] J. A. Aguilar-Saavedra and J. A. Casas, Eur. Phys. J. C **82**, 666 (2022).
[25] F. Maltoni, C. Severi, S. Tentori, and E. Vryonidou, J. High Energy Phys. 03 (2024) 099.
[26] A. J. Barr, Phys. Lett. B **825**, 136866 (2022).
[27] M. Fabbrichesi, R. Floreanini, E. Gabrielli, and L. Marzola, Eur. Phys. J. C **83**, 823 (2023).
[28] G. Aad *et al.* (ATLAS Collaboration), Nature (London) **633**, 542 (2024).
[29] A. Hayrapetyan *et al.* (CMS Collaboration), Phys. Rev. D **110**, 112016 (2024).
[30] F. Maltoni, C. Severi, S. Tentori, and E. Vryonidou, J. High Energy Phys. 09 (2024) 001.
[31] K. Ehatäht, M. Fabbrichesi, L. Marzola, and C. Veelken, Phys. Rev. D **109**, 032005 (2024).
[32] T. Han, M. Low, and Y. Su, J. High Energy Phys. 10 (2025) 217.
[33] B. Yang, Y. Zhang, Z. S. Wang, and X. Zhou, arXiv:2603.05846.
[34] P. Lo Chiatto, Phys. Rev. D **112**, 015017 (2025).
[35] K. Cheng, T. Han, and M. Low, Phys. Lett. B **868**, 139675 (2025).
[36] V. Durupt, F. Maltoni, and O. Mattelaer, J. High Energy Phys. 04 (2026) 103.
[37] M. M. Altakach, P. Lamba, F. Maltoni, and K. Sakurai, J. High Energy Phys. 07 (2026) 091.
[38] K. Cheng, T. Han, and M. Low, Phys. Rev. D **111**, 033004 (2025).
[39] H. W. Zhang, X. Cao, and T. F. Feng, Phys. Rev. D **113**, 114022 (2026).
[40] Y. C. Guo, T. Han, M. Low, and Y. Su, arXiv:2602.02719.
[41] T. Han, M. Low, N. McGinnis, and S. Su, J. High Energy Phys. 05 (2025) 081.
[42] L. Antozzi, E. Chalbaud, F. Déliot, F. Fabbri, M. C. N. Fiolhais, B. Fuks, A. Onofre, M. White, and P. Zhu, J. High Energy Phys. 06 (2026) 139.

[43] M. Duch, A. Strumia, and A. Titov, Eur. Phys. J. C **85**, 151 (2025).
[44] R. N. Mohapatra and R. E. Marshak, Phys. Rev. Lett. **44**, 1316 (1980); **44**, 1643(E) (1980).
[45] R. E. Marshak and R. N. Mohapatra, Phys. Lett. **91B**, 222 (1980).
[46] C. Wetterich, Nucl. Phys. **B187**, 343 (1981).
[47] A. Masiero, J. F. Nieves, and T. Yanagida, Phys. Lett. **116B**, 11 (1982).
[48] R. N. Mohapatra and G. Senjanovic, Phys. Rev. D **27**, 254 (1983).
[49] W. Buchmuller, C. Greub, and P. Minkowski, Phys. Lett. B **267**, 395 (1991).
[50] L. Randall and R. Sundrum, Phys. Rev. Lett. **83**, 3370 (1999).
[51] W. K. Wootters, Phys. Rev. Lett. **80**, 2245 (1998).
[52] J. F. Clauser, M. A. Horne, A. Shimony, and R. A. Holt, Phys. Rev. Lett. **23**, 880 (1969).
[53] J. S. Bell, Rev. Mod. Phys. **38**, 447 (1966).
[54] B. S. Cirelson, Lett. Math. Phys. **4**, 93 (1980).
[55] R. Horodecki, P. Horodecki, and M. Horodecki, Phys. Lett. A **200**, 340 (1995).
[56] A. Davidson, Phys. Rev. D **20**, 776 (1979).
[57] H. Davoudiasl, J. L. Hewett, and T. G. Rizzo, Phys. Rev. Lett. **84**, 2080 (2000).
[58] H. Davoudiasl, J. L. Hewett, and T. G. Rizzo, Phys. Rev. D **63**, 075004 (2001).
[59] H. Murayama, I. Watanabe, and K. Hagiwara, HELAS: HELicity amplitude subroutines for Feynman diagram evaluations, KEK Report No. KEK-91-11, 1992.
[60] J. Alwall, R. Frederix, S. Frixione, V. Hirschi, F. Maltoni, O. Mattelaer, H. S. Shao, T. Stelzer, P. Torrielli, and M. Zaro, J. High Energy Phys. 07 (2014) 079.
[61] P. Artoisenet, P. de Aquino, F. Demartin, R. Frederix, S. Frixione, F. Maltoni, M. K. Mandal, P. Mathews, K. Mawatari, V. Ravindran *et al.*, J. High Energy Phys. 11 (2013) 043.
[62] A. Das, P. S. B. Dev, Y. Hosotani, and S. Mandal, Phys. Rev. D **105**, 115030 (2022).
[63] Y. J. Fang, A. Bhoonah, K. Cheng, T. Han, Y. Liu, and H. Zhang, arXiv:2604.11887.